

POLITECNICO DI TORINO

Master Degree in Aerospace Engineering

Master Degree Thesis

# Nonlinear Dynamics and Control of an Aeroservoelastic System



**Supervisor:**

Prof. Giacomo Frulla

**Candidate:**

Irma Isnardi

External Supervisor:  
Dr. Sebastiano Fichera  
Dr. Paolo Paoletti

22 March 2018



The external supervisors are Dr. Sebastiano Fichera and Dr. Paolo Paoletti from the Department of Mechanical, Materials and Aerospace Engineering of the University of Liverpool.

# Summary

This work developed at the Department of Mechanical, Materials and Aerospace Engineering of the University of Liverpool concerns the study of nonlinear dynamics and control on an aeroelastic system. The aim of this work is to study the LCOs suppression in a nonlinear aeroelastic system through a feedback linearization and to study the subcritical bifurcation that the nonlinear system presents. The system considered is a wing section subject to a constant airflow in a wind tunnel test facility located at the University of Liverpool.

The increased wing flexibility has made the phenomenon of flutter and LCOs more important and control techniques to suppress these phenomena are required to enlarge the flight envelope beyond the natural flutter velocity. In this case the LCO is suppressed using a trailing edge flap; in fact the motion of this control surface modifies the aerodynamics loads, so that by regulating the flap it is possible to contrast the LCOs.

A two DOFs mathematical model will be developed, describing the aeroelastic system under study. This model will take into account the interaction of structural and elastic phenomena with the aerodynamic one. The structure will be modeled through a two DOFs plunge-pitch model with a structural nonlinearity; while an unsteady model will be used for aerodynamics.

The model will be tuned on experimental data to obtain a numerical model fitting, to describe appropriately the behaviour of the real system. Moreover the parameters of the nonlinearity will be obtained by a static experimental test on a nonlinear spring that is the structural nonlinearity of the real system.

The system open loop behaviour will be studied, considering first a linear system and determining flutter velocity. Then the structural non linearity will be added to the system so that a complete nonlinear system will be obtained. A comparison between the wind tunnel test simulation and the mathematical simulations will be done, and particular attention will be given to the subcritical bifurcation point, where we will study the unsteady behaviour of the system.

The control strategy applied to the system will be a partial feedback linearization technique to design a coordinates transformation and a nonlinear input by which is possible to linearize a part of the system. The linearized subsystem obtained

will be then made stable with the use of a linear control technique; in this case its poles are assigned via *pole-placement*. The control strategy will be implemented and applied in simulations to verify its effectiveness on a numerical model based on a real aeroelastic system. The effectiveness of the strategy will be tested by verifying the suppression of the LCOs in simulation.

# Sommario

Il lavoro di tesi è stato sviluppato presso il dipartimento di ingegneria dell'University of Liverpool e tratta lo studio della dinamica non lineare e del controllo di un sistema aeroelastico. L'obiettivo del lavoro di tesi è lo studio del punto di biforcazione subcritica e il ciclo limite che sono presenti nel sistema e il suo controllo tramite la feedback linearization. Il sistema aeroelastico considerato è un'ala a due gradi di libertà posta in galleria del vento.

L'aumento della flessibilità delle ali ha reso il fenomeno del flutter e dei cicli limite più significativi e le tecniche di controllo di questi fenomeni sono diventate necessarie per ampliare gli inviluppi di volo oltre le velocità critiche che i diversi sistemi presentano. Nel nostro sistema il ciclo limite viene soppresso grazie al flap presente sul bordo di fuga, che modifica il carico aerodinamico presente sull'ala e ne permette il controllo.

Basandosi sul modello sperimentale presente in galleria del vento, è stato sviluppato un modello matematico a due gradi di libertà, che ci permette di descrivere il sistema, definendo anche le iterazioni strutturali con l'aerodinamica. Per il modello struttura è stato costruito un modello flessione - torsionale con una non linearità strutturale, mentre per il modello aerodinamico è stato utilizzato un modello in stazionario.

I parametri del sistema lineare vengono quindi ottimizzati basandosi sui dati sperimentali e permettono di descrivere il comportamento del sistema in maniera più simile possibile al sistema reale. Anche i parametri della non linearità sono ottimizzati tramite dei test statici sulla molla non lineare presente sul modello in galleria del vento.

Inizialmente viene studiato il sistema lineare andando a determinare la velocità di flutter tramite un'analisi agli auto valori del sistema. Successivamente si aggiunge la non linearità sul grado di libertà flessionale ottenendo il sistema non lineare completo. A questo punto si vanno ad effettuare delle comparazioni tra i risultati teorici e quelli sperimentali, prestando particolare attenzione allo studio del punto di biforcazione subcritica che presenta il sistema.

La strategia di controllo applicata al sistema è la feedback linearization, una

delle tecniche più utilizzate per il controllo di sistemi non lineari. Questo controllo va a linearizzare parzialmente il sistema attraverso un ingresso non lineare. Una volta ottenuto il sotto sistema linearizzato è possibile controllarlo attraverso il riposizionamento dei poli del sistema. Il controllo è stato implementato sia sul modello matematico sia sul sistema reale in galleria del vento e testato per verificarne l'efficacia nel sopprimere il ciclo limite che presenta il sistema.

# Acknowledgements

Firstly, I would like to express my gratitude to my supervisors at University of Liverpool, Dr Sebastiano Fichera and Dr Paolo Paoletti, for giving me the unique opportunity to approach the research field and for the continuous support for my thesis work.

Secondly, I would like to thank my supervisor at Politecnico, Prof. Giacomo Frulla, in helping me especially during my thesis writing, for his availability and precious advice.

Apart from the people I worked with I would like to thank all the friends that improved my stay in Liverpool. In particular, I would like to thank Davide and Francesco who strongly helped me in settle in Liverpool. Thanks to them I met a lot of great people I became friend to, sharing great experience. Last but not least, I have to express my acknowledgement to Liam who sustained and helped me whenever I was in need.

Since this is not only the conclusion of my thesis, but it represents also the end of my studies I would like to thank also my friends at Politecnico, a particular thanks goes to Giancarlo, Gianluca and Simone my class-mates and co-workers and my two flat mates: Ornella for our talk and Carlotta my greatest supporter despite the distance.

Finally, I am sincerely grateful to my parents who strongly believe in my capabilities and they have given to me the opportunity to study.



# Contents

<b>Summary</b>	III
<b>Sommario</b>	V
<b>Acknowledgements</b>	VII
<b>List of Tables</b>	XI
<b>List of Figures</b>	XII
<b>List of Acronyms and Abbreviations</b>	XIV
<b>1 Mathematical Model</b>	1
1.1 Linear Structural Model . . . . .	2
1.2 Linear Aeroelastic Model . . . . .	4
1.3 State Variable Representation . . . . .	6
1.4 Nonlinear Model . . . . .	8
<b>2 Experimental Rig and Model Tuning</b>	11
2.1 Experimental Rig . . . . .	12
2.2 Parameters Estimation of the Linear System . . . . .	16
2.3 Nonlinear parameters estimation . . . . .	19
<b>3 Open loop behaviour</b>	21
3.1 Linear system behaviour . . . . .	21
3.2 Generic Nonlinear Aeroelastic Behaviour . . . . .	26
3.2.1 Nonlinear System Behaviour . . . . .	27
3.3 Subcritical bifurcation point . . . . .	30
3.3.1 The describing function method . . . . .	30
3.3.2 Application describing function method . . . . .	32

<b>4</b>	<b>Control Design and Closed-Loop Behaviour</b>	<b>37</b>
4.1	Feedback Linearization . . . . .	37
4.2	Feedback Linearization Applied to the Aeroelastic System . . . . .	40
4.2.1	Inner Dynamics . . . . .	44
4.2.2	Pole Placement via Feedback Linearization . . . . .	45
4.3	Simulink Design . . . . .	46
4.4	Closed-Loop Behaviour . . . . .	48
<b>5</b>	<b>Conclusions and Further Works</b>	<b>55</b>
	<b>Bibliography</b>	<b>57</b>

# List of Tables

2.1	2-DOFs rig geometrical characteristic. . . . .	12
2.2	. . . . .	14
2.3	Parameters dataset. . . . .	17
2.4	Nonlinear parameters dataset. . . . .	20



# List of Figures

1.1	Lateral view of the aerofoil subject to an airspeed $U$ .	2
1.2	2-DOFs aeroelastic system.	3
1.3	The real and imaginary part of Theodorsen's function $C(k)$ and Jones approximation.	6
2.1	Actuator construction: 1 - piezoelectric stacks [11].	12
2.2	Laser location on test rig [8].	13
2.3	Schematic representation of the laser position in the test rig.	13
2.4	Wind tunnel test section - view 1.	15
2.5	Wind tunnel test section - view 2.	15
2.6	Results from experimental model tuning for plunge DOF.	18
2.7	Results from experimental model tuning for pitch DOF.	19
2.8	Comparison between the experimental measures and the estimated polynomial.	20
3.1	Pitch and plunge DOFs damping.	22
3.2	Pitch and plunge DOFs natural frequency.	22
3.3	Aerodynamic states.	23
3.4	Pitch and plunge open loop response at $U = 10$ m/s.	24
3.5	Pitch and plunge velocities open loop response at $U = 10$ m/s.	25
3.6	Aerodynamic states open loop response at $U = 10$ m/s.	25
3.7	Schematic of LCO response [6].	26
3.8	Time domain LCO diagrams - numerical vs experimental.	28
3.9	Phase displacement between pitch and plunge.	29
3.10	Phase portraits - numerical vs experimental.	29
3.11	Feedback connection [10].	30
3.12	Plunge LCO amplitude.	34
3.13	Pitch LCO amplitude.	35
3.14	Plunge LCO frequency.	35
3.15	Pitch LCO frequency.	36
4.1	Schematic of control.	47

4.2	Test case 1: closed-loop response for 10% damping at 17 m/s. . . . .	49
4.3	Test case 1: closed-loop response for 20% damping at 17 m/s. . . . .	49
4.4	Test case 1: closed-loop response for 30% damping at 17 m/s. . . . .	50
4.5	Test case 1: flap motion for closed-loop response for 30% damping at 17 m/s. . . . .	50
4.6	Test case 2: closed-loop response for 30% damping and controller gain computed for 17 m/s at 15 m/s. . . . .	51
4.7	Test case 3: closed-loop response for 30% damping and controller gain computed for 15 m/s at 15 m/s. . . . .	52
4.8	Test case 4: closed-loop response for 30% damping and controller gain computed for 17 m/s at 19 m/s. . . . .	52

# List of Notation and Acronyms

Symbol(s)	Meaning [Units]
$h$	plunge displacement [m]
$\alpha$	pitch angle (or angle of attack of the airfoil) [rad]
$\beta$	angular deflection of the trailing edge control surface [rad]
$a$	non-dimensional distance between semi-chord and elastic axis, normalised by $b$ [-]
$b$	semi-chord of the airfoil [m]
$c$	chord of the airfoil [m]
$c_h$	plunge viscous damping coefficient [kgm <sup>2</sup> /s]
$c_\alpha$	torsional viscous damping coefficient about rotation axis [kg/s]
$I_\alpha$	moments of inertia of aerofoil section and other rotating parts about the rotation axis [kgm <sup>2</sup> /rad]
$k_h$	plunge stiffness [N/m]
$k_\alpha$	torsional stiffness about rotation axis [Nm/rad]
$m_T$	total mass of wing and its support structure [kg]
$m_w$	mass of the wing [kg]
$x_\alpha$	nondimensional distance of centre of mass of the airfoil from rotation axis, normalised by $b$ [-]
$U$	freestream speed [m/s]
$L$	aerodynamic lift [N]
$M$	aerodynamic moment [Nm]
$c_{l\alpha}, c_{m\alpha}$	lift and moment coefficients per angle of attack $\alpha$ [-]
$c_{l\beta}, c_{m\beta}$	lift and moment coefficients per control surface deflection $\beta$ [-]

c.g.	center of gravity
f.a. (or e.a.)	flexural axis (or elastic axis)
LCO(s)	Limit Cycle Oscillation(s)
FRF(s)	Frequency Response Function(s)
DOF(s)	Degree(s) Of Freedom



# Chapter 1

## Mathematical Model

In this chapter a mathematical model of the aeroelastic system with a structural nonlinearity is presented. The model describes the behaviour of a wing section at low speed airflow during a wind tunnel test.

The model is used to describe and analyse the motion of the system, in particular for estimating the flutter velocity. A definition of aeroelastic flutter is: *a dynamic instability of a flight vehicle associated with the interaction of aerodynamic, elastic, and inertial forces* [5]. Therefore, the flutter phenomenon arises when the aerodynamic force couples with a flexible body's natural frequency. This coupling induces an oscillatory motion with unbounded amplitude. In other word, flutter is a self-excited oscillatory instability and it could lead to a structural failure due to oscillatory motion with increasing amplitude. The presence of the structural nonlinearity affects the aeroelastic behaviour, for example our system in the structural hardening nonlinearity induces Limit Cycle Oscillations (LCOs), this response could be considered as bounded flutter.

In Section 1.1 the linear structural model is presented. The model is a 2-DOFs pitch and plunge model and the structural model is obtained via the classical Euler-Lagrange approach. In Section 1.2 at the system is coupled with an unsteady aerodynamic forcing. In Section 1.3 the model is written in a state space form that is the notation used to analysis and control the system. Finally, in Section 1.5 a fifth-order polynomial is added to the plunge DOF in the state space system to describe the non linear stiffness present in the experimental model.

## 1.1 Linear Structural Model

In this section a schematic representation of the real model is presented it is considered in the experimental validation, of Section 2.1. The test rig is schematically shown in Figure 1.1. The mathematical model derived in this section describes the behaviour of the test rig.

In this case this model is fully linear: the structure deformation is proportional to the applied forces, which could be static or dynamic. The structural nonlinearity will be added in the DOF plunge, in Section 1.5.

The dynamic of the system is described by a 2 DOFs model. The model considers a symmetric rigid aerofoil (NACA0018) with 2 DOFs. The translation motion (plunge) is described by the variable  $h$  that is defined as the distance between the elastic axis (e.a) in its undeformed position and e.a in the current position. The torsional motion (pitch) is described by the variable  $\alpha$  that is defined as the angle between chord line in undeformed position and chord line in current position. In this way, it is possible described the motion of each point of aerofoil as a combination of these two variable; in kinematic point of view system motion are represented. From the dynamic point of view it is necessary to consider at first inertial and elastic elements. Elastic elements are two springs that allow motion along the plunge and pitch DOFs: one translational spring allows  $h$  DOF (plunge) while one torsional spring allows  $\alpha$  DOF (pitch). The springs are attached to the same point on the aerofoil, as shown in Figure 1.1, and determinate the elastic axis, about which the aerofoil rotates.

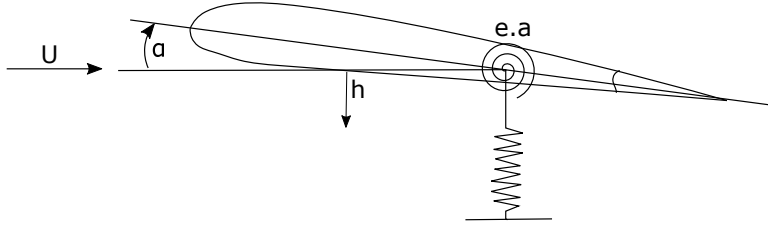


Figure 1.1: Lateral view of the aerofoil subject to an airspeed  $U$ .

It is possible determinate the mathematical model of the system with the Euler-Lagrange method. In order to simplify the calculations, the aerofoil shape is assumed to be flat plate as Figure 1.2, this is not too restrictive because the aerofoil is symmetric. Euler-Lagrange equation reads:

$$\frac{d}{dt} \left( \frac{\partial E_k}{\partial \dot{q}_i} \right) + \frac{\partial U}{\partial q_i} + \frac{\partial \Delta}{\partial \dot{q}_i} = Q_i \quad (1.1)$$

where  $q_i$  is a generalized coordinate and  $Q_i$  is the force applied to the  $i$ -th coordinate. In our case the generalized coordinates are the two DOFs:  $q_1 = h$ ,  $q_2 = \alpha$ .

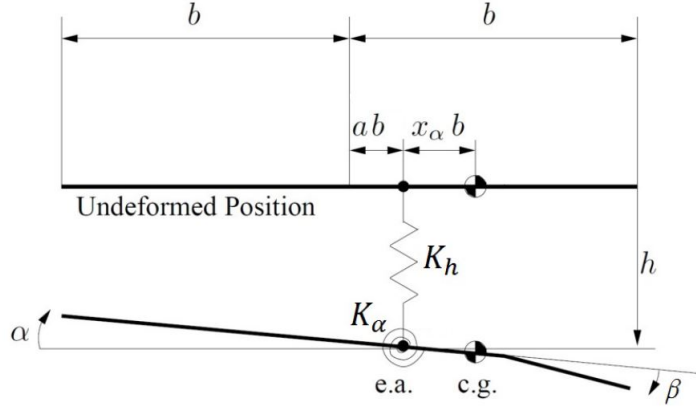


Figure 1.2: 2-DOFs aeroelastic system.

$x$  is measured along chord from e.a. and from the geometry it is possible to define the horizontal displacement of the aerofoil  $u$  and the vertical displacement  $w$ . By considering small pitch angle ( $\alpha \ll 1$ ) we obtain:

$$\begin{aligned} u &= x(\cos \alpha - 1) \simeq 0 \\ w &= -h - x \sin \alpha \simeq -h - x\alpha \end{aligned} \quad (1.2)$$

Hence, the kinetic energy is:

$$\begin{aligned} E_k &= \frac{1}{2} \int \left[ \left( \frac{dw}{dt} \right)^2 + \left( \frac{du}{dt} \right)^2 \right] \rho dx \simeq \frac{1}{2} \int \left( \frac{dw}{dt} \right)^2 \rho dx = \\ &= \frac{1}{2} m_t \dot{h}^2 + S_\alpha \dot{h} \dot{\alpha} + \frac{1}{2} I_\alpha \dot{\alpha}^2 \end{aligned} \quad (1.3)$$

where  $m_T = \int \rho dx$  is the total mass of the wing and its support structure.  $I_\alpha = \int \rho x^2 dx$  is the moment of inertia.  $S_\alpha = \int \rho x dx = m_w x_\alpha b$  is the mass unbalance.

The potential energy is:

$$U = \frac{1}{2} k_h h^2 + \frac{1}{2} k_\alpha \alpha^2 \quad (1.4)$$

where  $k_h$  and  $k_\alpha$  are the springs stiffnesses.

The damping is considered for movement of the two springs in a configuration mass-spring-damper. So it is possible write the dissipative energy,  $\Delta$ , as:

$$\Delta = \frac{1}{2} c_h \dot{h}^2 + \frac{1}{2} c_\alpha \dot{\alpha}^2 \quad (1.5)$$

where  $c_h$  and  $c_\alpha$  are the damper coefficients.

Finally,  $Q_h$  and  $Q_\alpha$  are the work done by the aerodynamic forces on the aerofoil that we presented in the next section.

Now, solving the Lagrange equation (1.1) for the two generalized coordinates  $h$  and  $\alpha$  gives:

$$\begin{bmatrix} m_T & S_\alpha \\ S_\alpha & I_\alpha \end{bmatrix} \begin{Bmatrix} \ddot{h} \\ \ddot{\alpha} \end{Bmatrix} + \begin{bmatrix} c_h & 0 \\ 0 & c_\alpha \end{bmatrix} \begin{Bmatrix} \dot{h} \\ \dot{\alpha} \end{Bmatrix} + \begin{bmatrix} k_h & 0 \\ 0 & k_\alpha \end{bmatrix} \begin{Bmatrix} h \\ \alpha \end{Bmatrix} = \begin{Bmatrix} -L \\ M \end{Bmatrix} \quad (1.6)$$

These equations describe the motion of the linear structural system and could be written in the standard notation for mass-spring-damper. It can be seen that while the stiffness matrix and the damping matrix are diagonal, the mass matrix is just symmetric, because of the terms  $S_\alpha$  coupling the two DOFs of the system.

At the end, it is possible to define the uncoupled natural frequencies of the system. In fact if  $S_\alpha$  and the damping coefficient are fixed to zero one obtains:

$$\omega_h = \sqrt{\frac{k_h}{m_T}} \quad \omega_\alpha = \sqrt{\frac{k_\alpha}{I_\alpha}} \quad (1.7)$$

## 1.2 Linear Aeroelastic Model

An airflow with velocity  $U$  affects an aerofoil. As shown in Figure 1.1, the airflow produces aerodynamic forces acting,  $p(x, t)$ , on any point of the structure which they interact with. It is possible describe the aerodynamic forces as lift  $L$  and moment  $M$ . The sign convention is that  $p(x, t)$  is positive up,  $L$  is positive up and  $M$  is positive nose up.

For describing the aerodynamic force we considered an unsteady aerodynamics, because the reduced frequency of the system reads  $k = \frac{\omega_\alpha b}{U} = 0.1$ . This parameter defines the degree of unsteadiness of the flow. If  $0 \leq k \leq 0.05$ , a system can be described by quasi-steady aerodynamics, if  $k \geq 0.05$  a system can be described by unsteady aerodynamics. The unsteady aerodynamic theory needs to account three separate physical phenomena:

1. The relative wind vector on the aerofoil is not fixed in space.
2. The aerofoil unsteady motion disturbs the flow and causes a vortex to be shed at the trailing edge.
3. The motion of the aerofoil accelerates air particles near the aerofoil surface.

The first and the second phenomena change the effective angle of attack and thus change the lift. The last one effect is less significant than the other and affects both lift and moment [5].

Theodorsen derived a theory of unsteady aerodynamics for a symmetric two-dimensional aerofoil and its derivation is based on linear potential-flow theory [7]. According to Theodorsen’s theory, lift and moment about the flexural axis can be written as:

$$L(t) = \pi \rho s_P b^2 \left( \ddot{h} + U \dot{\alpha} - ba \ddot{\alpha} \right) + 2\pi s_P \rho U b C(k) \left( \dot{h} + U \alpha + b \dot{\alpha} \left( \frac{1}{2} - a \right) \right) + \frac{T_{10} U s_P}{\pi} \beta \quad (1.8)$$

$$M(t) = \pi s_P \rho b^2 \left( ba \ddot{h} - Ub \left( \frac{1}{2} - a \right) \dot{\alpha} - \left( \frac{1}{8} + a^2 \right) \ddot{\alpha} \right) + (T_4 + T_{10}) U^2 s_P \beta + 2\pi s_P \rho U b^2 C(k) \left( \frac{1}{2} + a \right) \left( \dot{h} + U \alpha + b \dot{\alpha} \left( \frac{1}{2} - a \right) + \frac{T_{10} U s_P}{\pi} \beta \right) \quad (1.9)$$

where  $s_P$  is the span,  $T_{10}$  and  $T_4$  are described by Theodorsen and depend on the control surface hinge location:

$$T_{10} = \sqrt{1 - d^2} + \arccos(d) \quad T_4 = d\sqrt{1 - d^2} - \arccos(d) \quad (1.10)$$

The first part of each expression shows the noncirculatory terms and the second part shows the circulatory terms which are dependent upon the value of Theodorsen’s function,  $C(k)$ . The circulatory terms occurs due to the vorticity in the flow.

Theodorsen’s function is used to model the changes in amplitude and phase of the sinusoidal unsteady aerodynamic forces relative to the quasi-steady forces for different reduced frequencies. Theodorsen’s function is expressed as  $C(k) = F(k) + iG(k)$ , where  $C(k)$  is a complex quantity (required since both the amplitude and the phase need to change), is expressed as a function of reduced frequency such that:

$$C(k) = F(k) + iG(k) = \frac{H_1^{(2)}(k)}{H_1^{(2)}(k) + iH_0^{(2)}(k)} \quad (1.11)$$

where  $H_n^{(2)}(k)$  are Hankel functions of the second kind. The real part and imaginary part of Theodorsen’s function versus  $1/k$  are plotted in Figure 1.3. From the figure it is possible to notice that  $C(k) = 0.5$  for  $k \rightarrow +\infty$ , instead for the steady case, where  $k = 0$ ,  $C(k)$  is real and equal to  $C(k) = 1$ . When the terms are multiplied by  $C(k)$ , the function magnitude reduced and a phase lag is introduced [5].

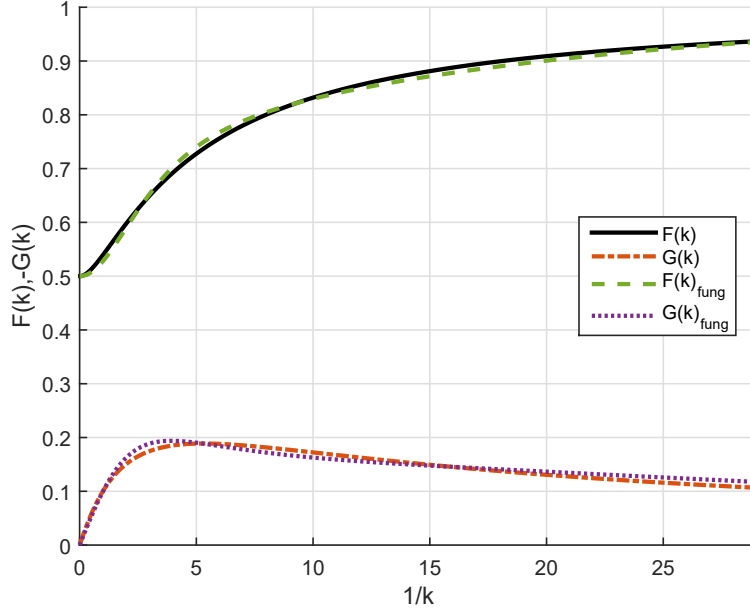


Figure 1.3: The real and imaginary part of Theodorsen's function  $C(k)$  and Jones approximation.

### 1.3 State Variable Representation

For control purpose it is necessary to rewrite the dynamics in a state space representation with real coefficients. The Theodorsen's function is complex. Therefore an approximation will be considered:

$$C(k) = 1 - \frac{0.165}{1 - \frac{0.0455}{k}i} - \frac{0.335}{1 - \frac{0.3}{k}i} \quad (1.12)$$

by replacing the reduced frequency  $k$  with  $\frac{sb}{U}$ ,  $s$  is the Laplace variable. Figure 1.3 shows the differences between the Theodorsen's function and the Jones's approximation. According to this approach,  $C(k)$  can be approximated as:

$$C(s) = 1 - \frac{0.165s}{s + 0.0455\frac{U}{b}} - \frac{0.335s}{s + 0.3\frac{U}{b}} = 0.5 + \frac{a_1s + a_0}{s^2 + b_1s + b_0} \quad (1.13)$$

where  $a_1 = 0.1080075\frac{U}{b}$ ,  $a_0 = 0.006825\frac{U^2}{b^2}$ ,  $b_1 = 0.3455\frac{U}{b}$ ,  $b_0 = 0.01365\frac{U^2}{b^2}$ .

The Theodorsen's function  $C(s)$  can be treated as a second-order transfer function of a filter with input

$$v_f(t) = U\alpha + \dot{h} + b\left(\frac{1}{2} - a\right)\dot{\alpha} = a_v^T x_p \quad (1.14)$$

where the partial state vector reads  $x_p = \left[ h \quad \alpha \quad \dot{h} \quad \dot{\alpha} \right]^T \in \mathbb{R}^4$  and the vector  $a_v \in \mathbb{R}^4$  is defined as

$$a_v = \left[ 0 \quad \alpha \quad \dot{h} \quad b\left(\frac{1}{2} - a\right) \right]^T \quad (1.15)$$

The output of the filter is denoted as  $y_f(t)$  which is related to input  $v_f(t)$  as

$$\hat{y}_f(s) = C(s)\hat{v}_f(s) \quad (1.16)$$

where  $\hat{y}_f(s)$  and  $\hat{v}_f(s)$  represent Laplace transforms of  $y_f(t)$  and  $v_f(t)$ , respectively. Note that the input to the filter  $C(s)$  is a linear combination of the plunge and pitch variables, i.e the structural DOFs of the system.

The transfer function  $C(s)$  of the filter has a minimal realization of dimension two. Although one can derive a variety of equivalent realizations of  $C(s)$ , we consider a representation of the filter of the form

$$\dot{x}_{f1} = x_{f2} \quad (1.17)$$

$$\dot{x}_{f2} = v_f - b_0 x_{f1} - b_1 x_{f2} \quad (1.18)$$

with its output given by

$$y_f = \frac{1}{2}v_f + a_0 x_{f1} + a_1 x_{f2} \quad (1.19)$$

Finally, it is possible define the state vector including the filter state as:

$$x = \left[ h \quad \alpha \quad \dot{h} \quad \dot{\alpha} \quad x_{f1} \quad x_{f2} \right]^T = \left[ x_1 \quad x_2 \quad x_3 \quad x_4 \quad x_5 \quad x_6 \right]^T \quad (1.20)$$

Now it is possible write the lift  $L(t)$  and moment  $M(t)$  in (1.8) and (1.9) as:

$$L(t) = 2\pi s_P \rho U b y_f \left( \dot{h} + U\alpha + b\dot{\alpha} \left( \frac{1}{2} - a \right) \right) + \pi s_P \rho b^2 \left( \ddot{h} + U\dot{\alpha} - ba\ddot{\alpha} \right) + \frac{T_{10} U s_P}{\pi} \beta \quad (1.21)$$

$$M(t) = \pi \rho s_P b^2 \left( ba\ddot{h} - Ub \left( \frac{1}{2} - a \right) \dot{\alpha} - b^2 \left( \frac{1}{8} + a^2 \right) \ddot{\alpha} \right) + (T_4 + T_{10}) s_P U^2 \beta + 2\pi s_P \rho U b^2 y_f \left( \frac{1}{2} + a \right) \left( \dot{h} + U\alpha + b\dot{\alpha} \left( \frac{1}{2} - a \right) + \frac{T_{10} U s_P}{\pi} \beta \right) \quad (1.22)$$

Substituting the aerodynamics forces, Eq. (1.21) and Eq. (1.22) in Eq. (1.6), and collecting the terms involving  $\ddot{h}$  and  $\ddot{\alpha}$  and solving for them gives:

$$\begin{bmatrix} \ddot{h} \\ \ddot{\alpha} \end{bmatrix} = A_1 x + B_1 \beta \quad (1.23)$$

where  $A_1 \in \mathbb{R}^{2 \times 6}$  and  $B_1 \in \mathbb{R}^2$ . The matrix  $A_1$  could be divided in three different submatrices:

$$[A_1] = \begin{bmatrix} -[M]^{-1}[D] & -[M]^{-1}[K] & -[M]^{-1}[F] \end{bmatrix} = \begin{bmatrix} [P] & [Q] & [R] \end{bmatrix} \quad (1.24)$$

where  $[M]$  is the structural and aerodynamic inertia,  $[D]$  is the structural and aerodynamic damping,  $[K]$  is the structural and aerodynamic stiffness and  $[F]$  contains the parameters that depend by new states.

Now the model (1.23) is linear respect the two variables pitch and plunge and their first, so we can rewrite it in a state variable representation:

$$\dot{x} = \begin{bmatrix} 0 & 0 & 1 & 0 & 0 & 0 \\ 0 & 0 & 0 & 1 & 0 & 0 \\ q_1 & q_2 & p_1 & p_2 & r_1 & r_2 \\ q_3 & q_4 & p_3 & p_4 & r_3 & r_4 \\ 0 & 0 & 0 & 0 & 0 & 1 \\ 0 & U & 1 & b(0.5 - a) & -b_0 & -b_1 \end{bmatrix} x + \begin{bmatrix} 0 \\ 0 \\ g_3 \\ g_4 \\ 0 \\ 0 \end{bmatrix} \beta = Ax + B\beta \quad (1.25)$$

where  $q_i$ ,  $p_i$ ,  $r_i$  are the element inside  $A_1$ . The equation of motion include aerodynamic forces which are nonlinearly dependent on the freestream velocity. So the behaviour of the system is depending on the airflow velocity.

## 1.4 Nonlinear Model

In this section a structural nonlinearity is incorporated into the system in the form of a hardening polynomial stiffness in the plunge DOF. This is achieved in the experimental by a clamped-clamped tensioned wire, as described in 2.1. Therefore a fifth-order polynomial nonlinearity is added in the mathematical model to the plunge DOF to describe the nonlinear stiffness induced by the tensioned wire:

$$k_h(h) = k_0 + k_2 h^2 + k_4 h^4 \quad (1.26)$$

where  $k_1$ ,  $k_3$  and  $k_5$  are estimated via a static force/displacement test as explained in the next chapter.

In Eq. (1.26) it is possible observe that as the stiffness increases as the displacement increases. Introducing such nonlinearity in the space state, Eq. (1.25), the complete nonlinear aeroelastic system is obtained:

$$\dot{x} = f(x) + B\beta \quad (1.27)$$

where:

$$f(x) = \begin{pmatrix} x_3 \\ x_4 \\ (\tilde{q}_1 + f_{nl1}(x_1))x_1 + q_2x_2 + p_1x_3 + p_2x_4 + r_1x_5 + r_2x_6 \\ (\tilde{q}_3 + f_{nl3}(x_1))x_1 + q_4x_2 + p_3x_3 + p_4x_4 + r_3x_5 + r_4x_6 \\ x_6 \\ Ux_2 + x_3 + b(0.5 - a)x_4 - b_0x_5 - b_1x_6 \end{pmatrix} \quad (1.28)$$

The terms  $\tilde{q}_1$  and  $\tilde{q}_3$  include  $k_0$ , the linear part of the nonlinear spring stiffness. In this way it is possible to isolate the nonlinear functions  $f_{nl1}(x_1)$  and  $f_{nl3}(x_1)$ , and the system could be written as:

$$\dot{x} = Ax + f_{nl}\psi(h) + B\beta \quad (1.29)$$

where  $\psi(h) = k_2h^3 + k_4h^5$  is the structural nonlinearity.



## Chapter 2

# Experimental Rig and Model Tuning

In this chapter the experimental rig and the identification method of the system are presented. The experimental setup used for the validation of the numerical model presented in Chapter 1 is a 2-DOF pitch-plunge aerofoil section. Hereinafter the geometrical characteristics of the experimental model are presented together with the used for introducing the structural hardening nonlinearity. These topics are also presented in ref. [1], but in the following they will be elaborated more and new elements will be added.

An identification method was required to determine the structural parameters of the model that was not possible to measure directly on the test rig. The resulting mathematical model describes as accurately as possible the behaviour of the physical model. The model tuning is performed by collecting multiple experimental FRFs (Frequency Response Function), and then using them as objective for a least square optimisation for the initial elastic model. Once the elastic model is tuned it is possible to add the other contributions like the aerodynamic force and the nonlinearity. This is possible since the system can be break-down into subsystems by removing the aerodynamics for analyzing the structural part. A *grey-box* approach has been chosen to describe what is the known of the physical system in the identification. In this case the model tuning is applied only to estimate the structural parameters that are unknown or uncertain.

In the first part of the chapter the test rig is presented. In the second part of the chapter the identification of the linear system is considered. In the last part is presented how the nonlinearity parameters are estimated.

## 2.1 Experimental Rig

The experimental setup is a rigid wing represent a 2-DOFs pitch-plunge aerofoil section installed in a slow-speed wind tunnel at the University of Liverpool. The wind tunnel presents a test section of  $1.2 \times 1.6$  m and a maximum flowstream velocity of 20 m/s. The aeroelasticity is shown in Figures 2.4 and 2.5. The geometric characteristics of the aerofoil are summarized in the Table 2.1. The aerofoil section is supported by horizontal and vertical linkages and a torque tube, this solution prevents spanwise tilting or bending. The aerofoil section has a NACA 0018 profile; the wing has a trailing edge flap in the center coverly 30% of the span. The flap can rotate of  $\pm 5$  deg, up to a bandwidth of 15 Hz; the flap can over work up to 30 Hz at lower amplitude. In the experimental validation, the control surface was commanded in closed loop with saturation of  $\pm 3$  deg. The plunge and pitch stiffness are introduced independently in both direction by adjustable leaf springs. The structural nonlinearity is added in the plunge DOF through a clamped-clamped wire arrangement in the form of a hardening polynomial stiffness form [8].

wing	
chord	0.35 m
span	1.2 m

flap section	
chord	0.0875 m
span	0.42 m

Table 2.1: 2-DOFs rig geometrical characteristic.

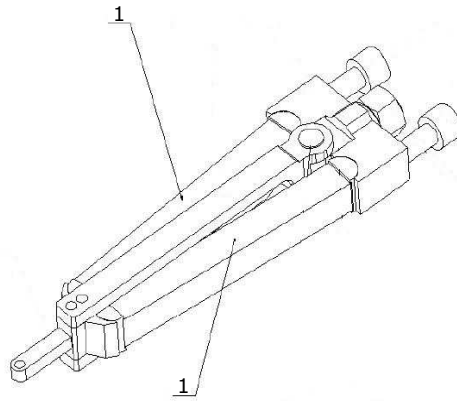


Figure 2.1: Actuator construction: 1 - piezoelectric stacks [11].

A dSPACE real-time control system is used for closed-loop control. The inputs to dSPACE are the voltages from three laser displacement sensors opportunely located, as shown in Figure 2.2. The control output from dSPACE is amplified by two amplifiers to the "V-stack" piezoelectric stack arrangement that activates the trailing edge flap on the wing. Two amplifiers are needed because the actuator is composed by twin piezostacks oriented as a "V", hence the name: V-stack. The flap moves when one piezostack extends meanwhile the other retracts by the same measure, this is achieved by powering the same voltages to two piezostack but out of phase of 180 deg [8].

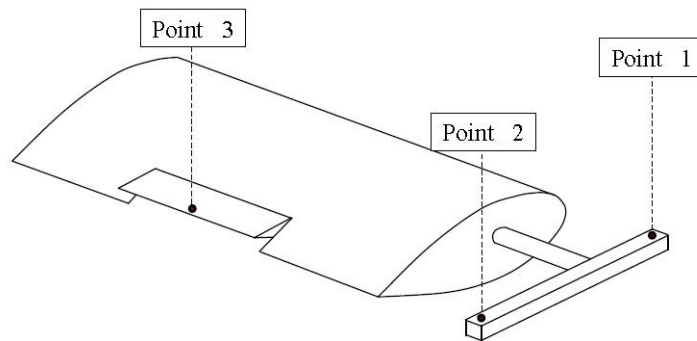


Figure 2.2: Laser location on test rig [8].

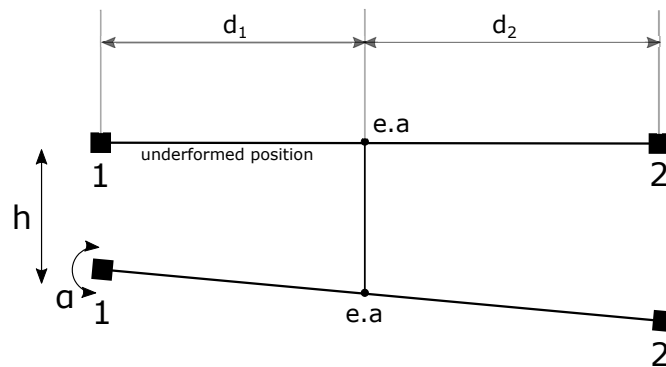


Figure 2.3: Schematic representation of the laser position in the test rig.

The flap is the input to the system during closed-loop and its the control law, is calculated through the partial feedback linearization technique presented in Chapter 4. Plunge and pitch deflections are mesured, their velocities, plus the two aerodynamic states are reconstructed in real-time, the latter by the last two rows of the

equation (1.25).

The deflections are obtained by geometrical relations between the positions of the lasers in point 1 and point 2. Figure 2.1 shows a schematic representation of the elements that permit the measurement of the displacements. From Figure 2.3 is possible to determinate the geometrical relations between the displacement measured by the lasers and the pitch and plunge measurement:

$$h = y_2 + (y_1 - y_2) \frac{d_1}{d_1 + d_2} \quad (2.1)$$

$$\alpha = \arctan \left( \frac{y_1 - y_2}{d_1 + d_2} \right) \quad (2.2)$$

Where  $y_1$  is the displacement measured by the laser in the point 1 and  $y_2$  is the displacement measured by the laser in the point 2.  $d_1$  and  $d_2$  are the distances between the elastic axes (e.a.) and the point 1 and point 2 respectively. In this way plunge ( $h$ ) and pitch ( $\alpha$ ) are obtain. The velocities are then numerically derived.

All the displacement readings are numerically filtered with a second order Butterworth filter with a cutoff frequency of 15 Hz. Figures 2.4 and 2.5 show the test rig where are pointed the most important elements, already described in detailed and they are referred also in the following Table 2.1.

- (a) laser displacement sensors
- (b) torsion bar
- (c) aerofoil section
- (d) trailing edge control surface
- (e) pitch spring
- (f) plunge spring - nonlinear
- (g) aerofoil vertical support
- (h) plange spring - linear

Table 2.2

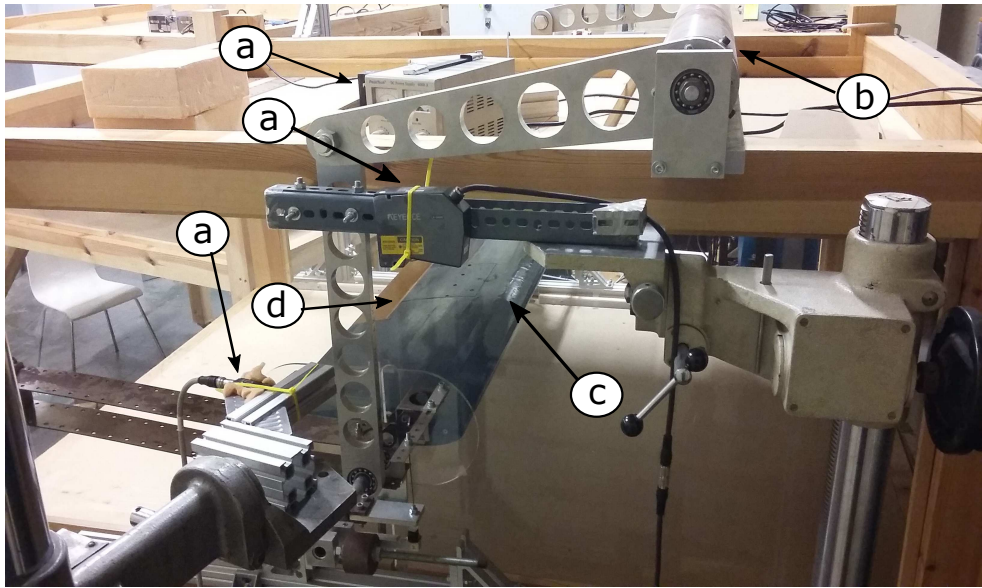


Figure 2.4: Wind tunnel test section - view 1.

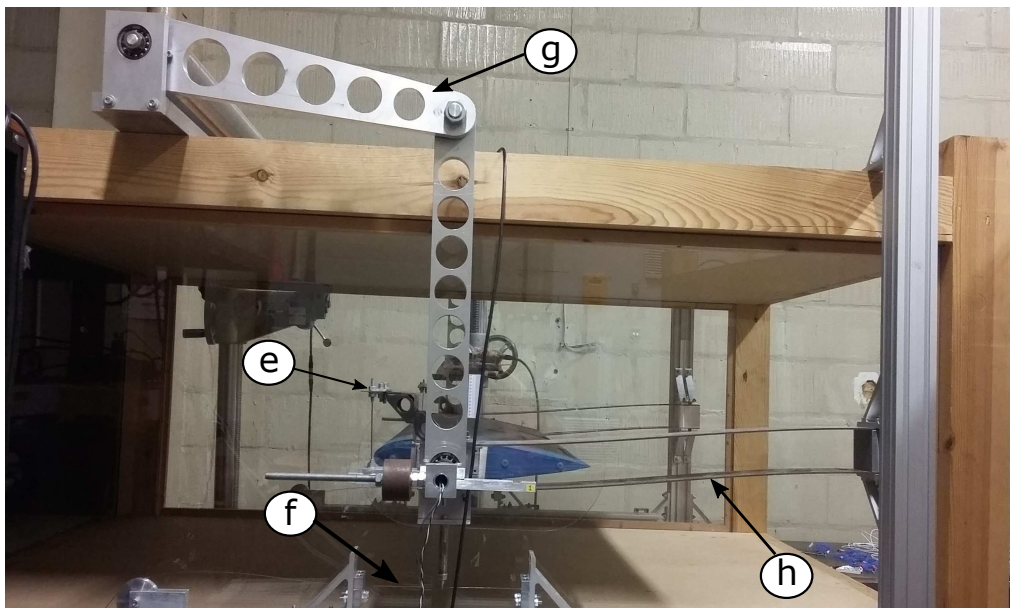


Figure 2.5: Wind tunnel test section - view 2.

## 2.2 Parameters Estimation of the Linear System

The linear system described in Eq. (1.6), without the aerodynamic forcing  $L$  and  $M$ , is written in the standard form of a mass-spring-damper coupled system. If a harmonic force is applied to the system, its response is related to the parameters that describe the physical model. The response of the system is formed by two terms: the general solution (or the transient response) and the particular solution (or the steady state response). The solutions are two functions in time domain, one for each DOF, but the identification method needs a response in the frequency domain and it is possible derived the analytical transfer function from the physical model. The model tuning is made by the comparison between the analytical and the experimental transfer functions. The last one are reconstructed collecting several experimental FRFs of the system. As already explained, the identification method start from a certain parameters dataset and adjust them to fit analytical transfer functions to the experimental one. In this case, the fitting is made solving the problem as a nonlinear least squares problem minimizing the least squares of the errors of each data point. This identification is classified as a grey-box approach because it uses a priori knowledge of the physical system.

In this case, for computing the two FRFs, the system is excited with a known force ( $F$ ) applied on the plunge DOF with a shaker. All the tests are carried out with the deflection constrained. The tests can be described in a mathematical model by considering the linear system, Eq. (1.6) without the aerodynamic forcing, but with a sinusoidal force  $F$  on the plunge DOF.

$$\begin{bmatrix} m_T & S_\alpha \\ S_\alpha & I_\alpha \end{bmatrix} \begin{Bmatrix} \ddot{h} \\ \ddot{\alpha} \end{Bmatrix} + \begin{bmatrix} c_h & 0 \\ 0 & c_\alpha \end{bmatrix} \begin{Bmatrix} \dot{h} \\ \dot{\alpha} \end{Bmatrix} + \begin{bmatrix} k_h & 0 \\ 0 & k_\alpha \end{bmatrix} \begin{Bmatrix} h \\ \alpha \end{Bmatrix} = \begin{Bmatrix} F \\ 0 \end{Bmatrix} \quad (2.3)$$

By applying the Laplace transform to the system, Eq. (2.3), we obtain for each DOF an FRF. The overall system is described by two linear systems: the first relative to plunge DOF with input pitch DOF and the force, the second relative to pitch DOF with input plunge DOF:

$$H(s) = -\frac{S_\alpha s^2}{m_T s^2 + c_h s + k_h} A(s) + \frac{F(s)}{m_T s^2 + c_h s + k_h} \quad (2.4)$$

$$A(s) = -\frac{S_\alpha s^2}{I_\alpha s^2 + c_\alpha s + k_\alpha} H(s) \quad (2.5)$$

where  $H(s) = \mathcal{L}\{h(t)\}$  and  $A(s) = \mathcal{L}\{\alpha(t)\}$ . It is possible to rewrite the transfer function as:

$$H(s) = \frac{I_\alpha s^2 + c_\alpha s + k_\alpha}{(m_T s^2 + c_h s + k_h)(I_\alpha s^2 + c_\alpha s + k_\alpha) - S_\alpha^2 s^4} F(s) \quad (2.6)$$

$$A(s) = -\frac{S_\alpha s^2}{(m_T s^2 + c_h s + k_h)(I_\alpha s^2 + c_\alpha s + k_\alpha) - S_\alpha^2 s^4} F(s) \quad (2.7)$$

The two transfer functions have the same four poles and so the overall system has two couples of poles.

The initial set of parameters is chosen based on direct and indirect test rig measures: the linear spring stiffness,  $k_h$  and  $k_\alpha$ , are measured from a static force/displacement test. The natural frequency and the damping ratio are measured from a model analysis test. The terms  $x_\alpha$  and  $m_w$  are measured by a static moment test with pitch spring disconnected. The resulting initial parameters dataset, and the optimized ones are reported in Table 2.3. It was necessary to consider several trails varying in a reasonable range the initial dataset to avoid local minimum. In fact, for model tuning algorithms, local minima are possible and the several trails allow the convergence to the global minimum. The initial dataset was chosen to obtain the smallest residuals possible. Figures 2.6 and 2.7 show the resulting FRFs obtained from the

	Initial parameters	Optimized parameters
$m_T$ [kg]	10.6956	12.4518
$m_w$ [kg]	5.0260	6.2168
$I_\alpha$ [kgm <sup>2</sup> /rad]	0.0382	0.0404
$x_\alpha$ [–]	0.0186	0.0230
$\zeta_k$ [–]	0.0128	0.0183
$\zeta_\alpha$ [–]	0.0174	0.0082
$k_h$ [N/m]	2930	3514.8
$k_\alpha$ [Nm/rad]	32.4297	33.6299

Table 2.3: Parameters dataset.

experimental model tuning at zero speed. In the Figures, there are the comparisons between the initial estimation (green dashed lines) and the experimental FRFs data (black dotted lines), and the optimized estimation (purple solid lines). There are some differences between the initial dataset and the experimental FRFs, while in average the discrepancy becomes smaller between the estimated FRFs and the experimental one as expected. The fit is more precise about the peaks and the larger values because they are associated to bigger residual values, so their fit gives a larger contribution on reducing the overall error.

Furthermore we can determine the system frequency which are defined in the peaks present in the FRFs. From Figures 2.6 and 2.7, we note that the first peak is the natural frequency of the plunge DOF at 16.65 rad/s and second one is the pitch natural frequency at 28.90 rad/s, the frequencies obtain depend by the mass unbalance  $S_\alpha$  and by damping coefficients, then they will be different from the uncoupled natural frequencies defined in 1.7:

$$\omega_h = \sqrt{\frac{k_h}{m_T}} = 16.80 \text{ rad/s} \quad \omega_\alpha = \sqrt{\frac{k_\alpha}{I_\alpha}} = 28.85 \text{ rad/s}$$

The difference between the natural frequencies uncoupled and coupled is small, but it can be notice that the two peak move away from each other. Figure 2.6 shows the FRF plunge DOF, where the peak of the natural plunge frequency it is well defined, while the pitch frequency peak it is small, then the two DOFs in this case are slightly coupled. On the contrary, Figure 2.7 shows the FRF pitch DOF, where both frequency peaks are well defined, so in this case the two are coupled in a strong way.

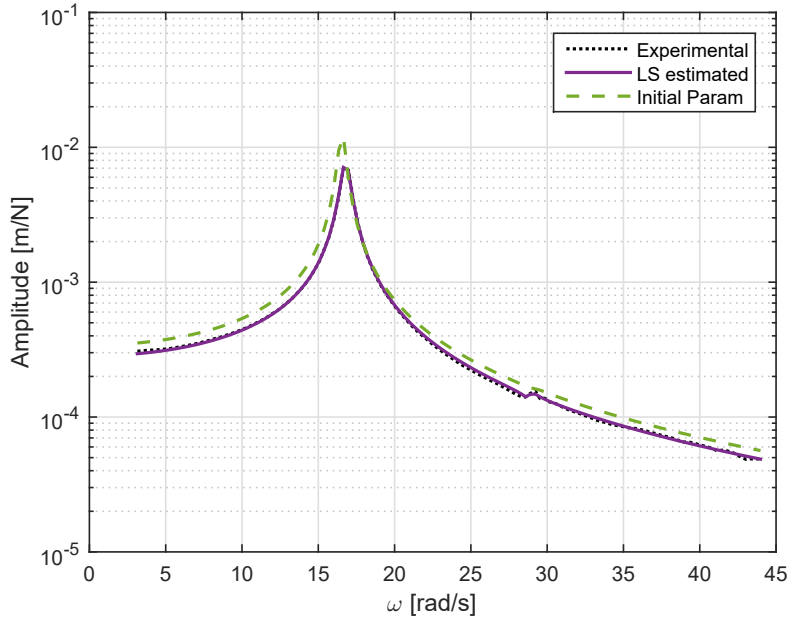


Figure 2.6: Results from experimental model tuning for plunge DOF.

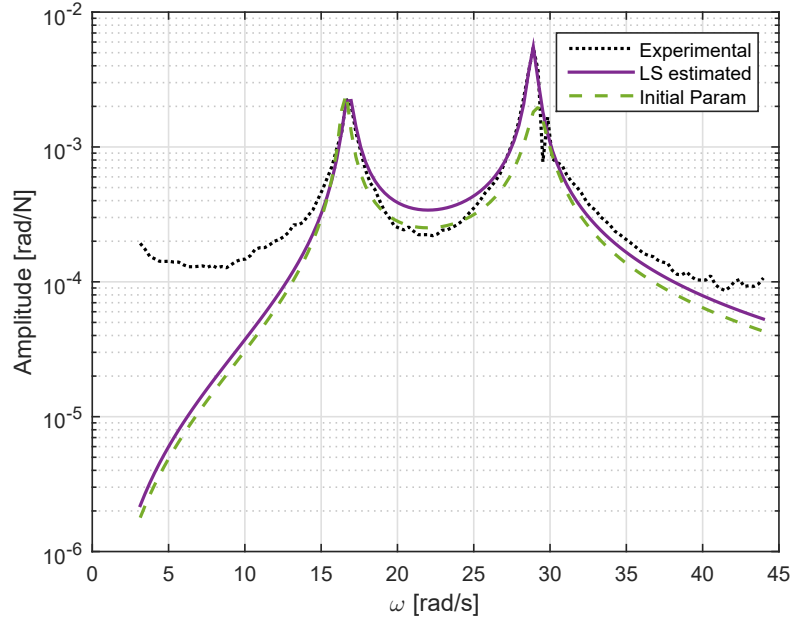


Figure 2.7: Results from experimental model tuning for pitch DOF.

## 2.3 Nonlinear parameters estimation

In this section the estimation of the stiffness parameters of the nonlinear springs is presented. The nonlinearity used is a pretensioned, clamped-clamped wire attached to the plunge DOF, as explain in Section 2.1. The stiffness parameters of a nonlinear spring are considered to be in a polynomial form:

$$k_h(h) = k_{h0} + k_{h1}h + k_{h2}h^2 + k_{h3}h^3 + k_{h4}h^4 + k_{h5}h^5 + \dots \quad (2.8)$$

In this case, a fifth-order polynomial nonlinearity is considered. It is possible to write the mathematical model of a pretensioned clamped-clamped wire used for introduced the nonlinearity in the test rig:

$$F = \frac{4T_0}{L}\delta + \frac{8}{L^3}(EA - T_0)\delta^3 - \frac{16EA}{L^5}\delta^5 \quad (2.9)$$

where  $T_0$  is the wire pretension, in our case the pretension is 1 kg,  $L$  is length of wire,  $E$  is elastic modulus,  $A$  is the wire section and  $\delta$  is the displacement. The parameters are estimated from the measurement by fitting the data with a polynomial fifth-order curve. The resulting parameters dataset are shown in Table 2.4 and a comparison of the estimated curve and the experimental data points are shown in Figure 2.8.

$k_{h0}$ [N/mm]	0.1987
$k_{h2}$ [N/mm <sup>3</sup> ]	0.1066
$k_{h4}$ [N/mm <sup>5</sup> ]	$1.2760e - 3$

Table 2.4: Nonlinear parameters dataset.

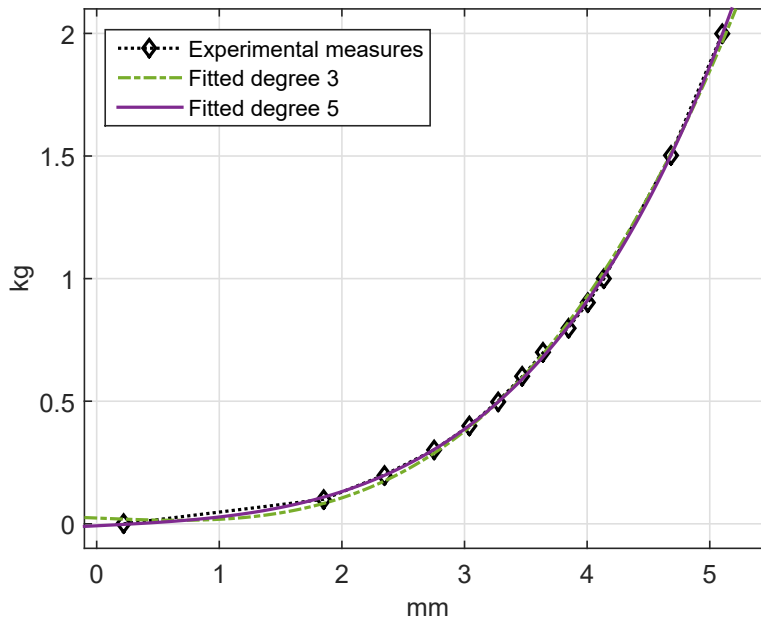


Figure 2.8: Comparison between the experimental measures and the estimated polynomial.

# Chapter 3

## Open loop behaviour

In this chapter the behavior of the open loop system is analyzed. In the first step the linear system was considered and an eigenvalue analysis was performed to determine the natural frequencies and the damping coefficients of the modes of the system. With this analysis is possible to determine the flutter velocity that is a threshold for the behaviour of the system; the aeroelastic wing such velocity is stable under and unstable above it. The time responses of the linear system have been studied, too. In the second part of the chapter, the nonlinear system was analysed. If in the linear system the instability can be completely described as divergent behavior, in nonlinear case, something different could happens. In fact the system can have different points of equilibrium, such as LCO. However, in the nonlinear case, specific nonlinear methods like describing functions have to be used for a more accurate analysis.

### 3.1 Linear system behaviour

The linear system response depends on the airflow velocity  $U$ , once the aerodynamic forces are added to the structural model. In this section, it will be considered the linear system in state space, to which the filter filtered in section 1.3 has already been applied.

Eigenvalues analysis is exploited at different freestream velocity, the results are shown in Figures 3.1, 3.2, 3.3. The airflow range of interest is between 0-25 m/s; the system's eigenvalues are six, the first four are two complex conjugate pairs, and each pair is associated to one DOF: the real part describes the system damping and the imaginary part describes the system natural frequency. The last two eigenvalues are real and describes the behavior of the two new aerodynamic states added in Section 1.3.

Figures 3.1 and 3.2 show the behaviour of the four complex conjugate eigenvalues.

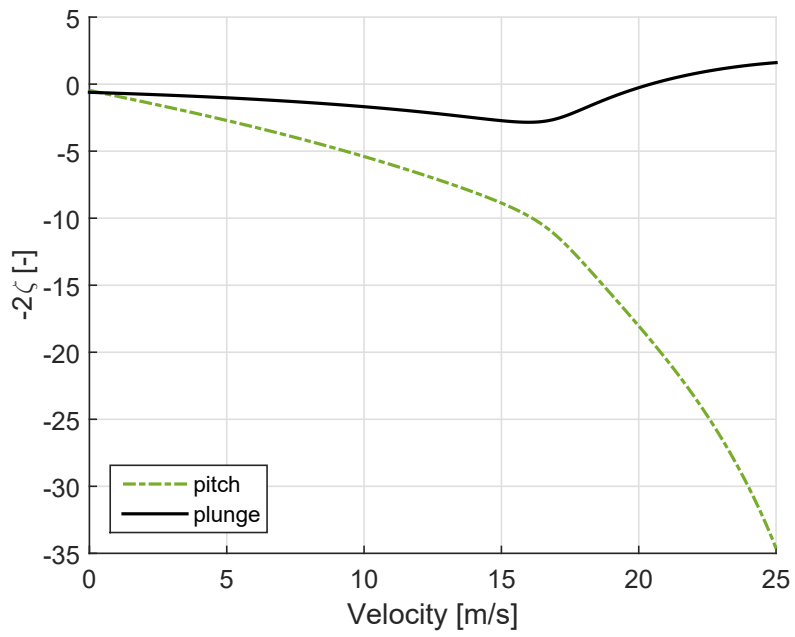


Figure 3.1: Pitch and plunge DOFs damping.

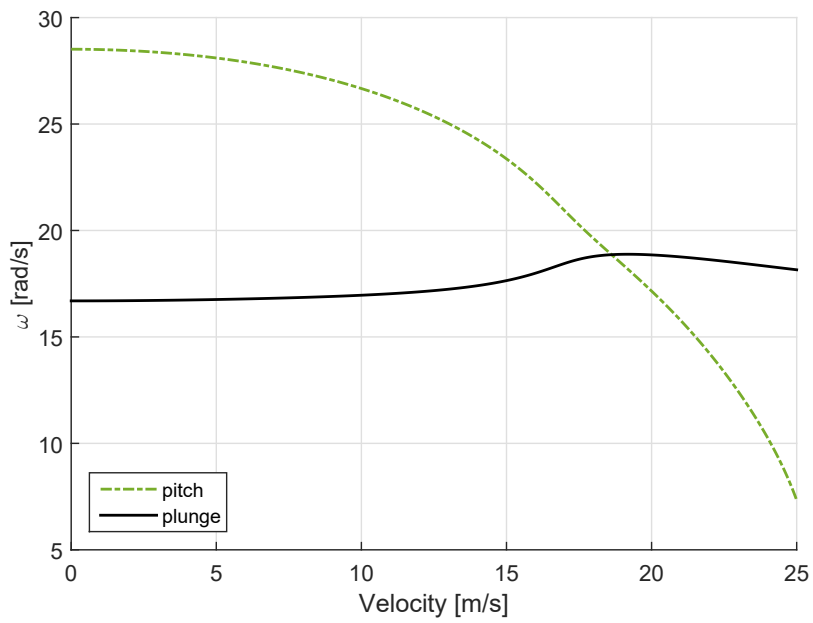


Figure 3.2: Pitch and plunge DOFs natural frequency.

In Figure 3.1, the system damping is represented and it is possible to see that a branch of the graph becomes positive, determining a flutter velocity at 20.3 m/s. Meanwhile, the other branch increases its modulus and so its stability. In Figure 3.2 there is presented the system frequencies, where the pitch frequency decreases with the velocity and plunge one increases. The two frequencies crossed shortly before the flutter velocity. Finally, it is possible to notice that at zero speed the system damping is the structural damping, and, similarly, in the same way the system frequencies are coupled natural frequencies of the system, as defined in Section 2.2. If we consider the frequency domain, we observe the peaks of the coupled natural frequencies, as presented in Figures 2.7 and 2.6 at zero speed. With increasing speed, the two peaks approach each other, until they collapsed in a single peak, i.e. in an undefined single mode. After the two frequencies cross each other, they move away, this situation happens near the flutter velocity.

The numerical flutter velocity  $U_f = 20.3$  m/s is very close to the experimental one  $U_{f,exp} = 19.4$  m/s [8], the error between the two flutter velocities is below 5%.

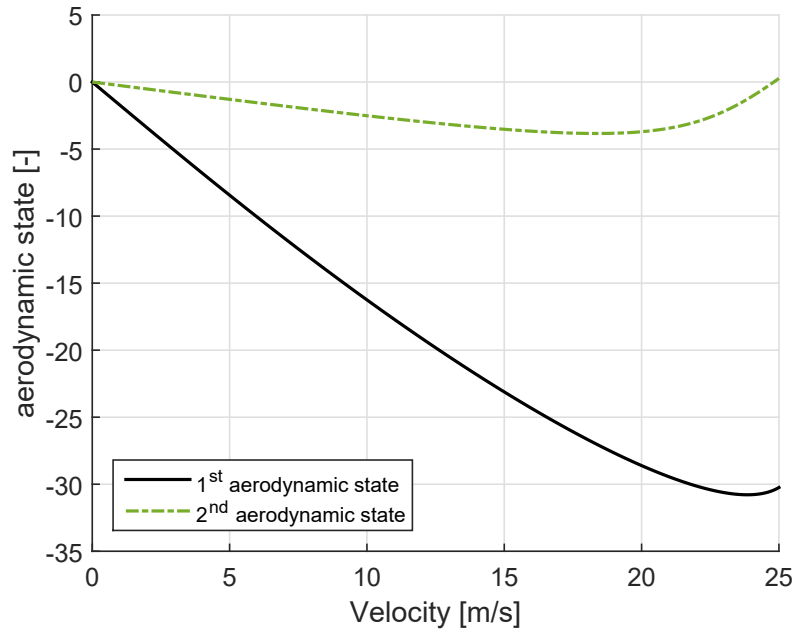


Figure 3.3: Aerodynamic states.

Figure 3.3 describes the behaviour of the aerodynamics states, they are null at zero speed and become negative while increasing the airspeed. The second aerodynamic state becomes positive near 25 m/s, but the system is already unstable, the flutter velocity is already exceeded, hence it is not relevant for studying the system behaviour.

Figures 3.4, 3.5 and 3.6 present the time responses of the system at airflow velocity lower than the flutter one, due to a perturbation of the pitch angle of  $5^\circ$  as shown in Figure 3.4. The system is stable and all the state converge to the origin in small period of time in accordance to their damping. The two aerodynamic states are impossible to observe directly on the model, but in any case are stable, as expected after the study of the eigenvalues of the system.

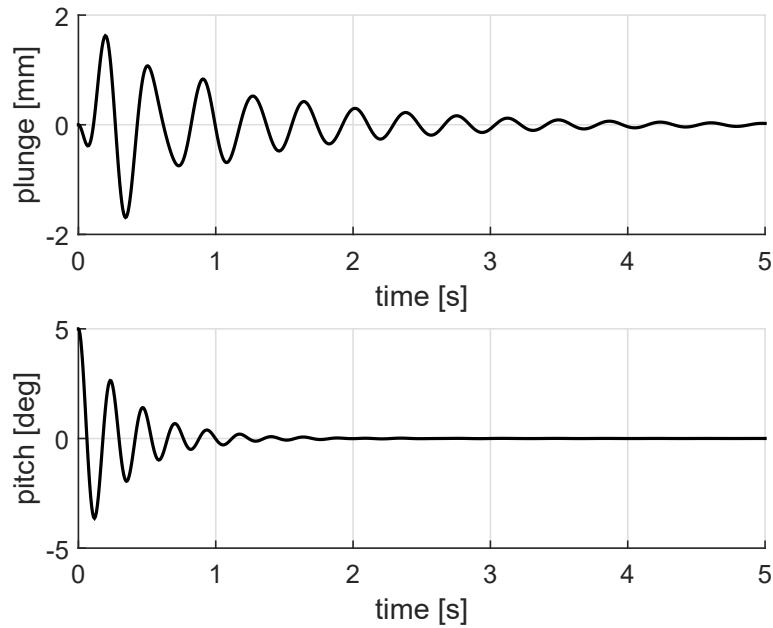


Figure 3.4: Pitch and plunge open loop response at  $U = 10$  m/s.

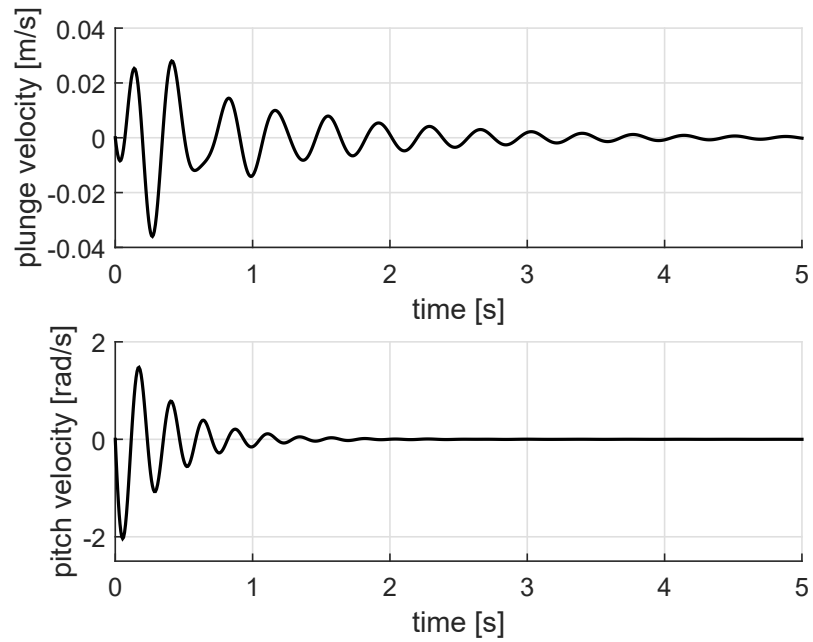


Figure 3.5: Pitch and plunge velocities open loop response at  $U = 10$  m/s.

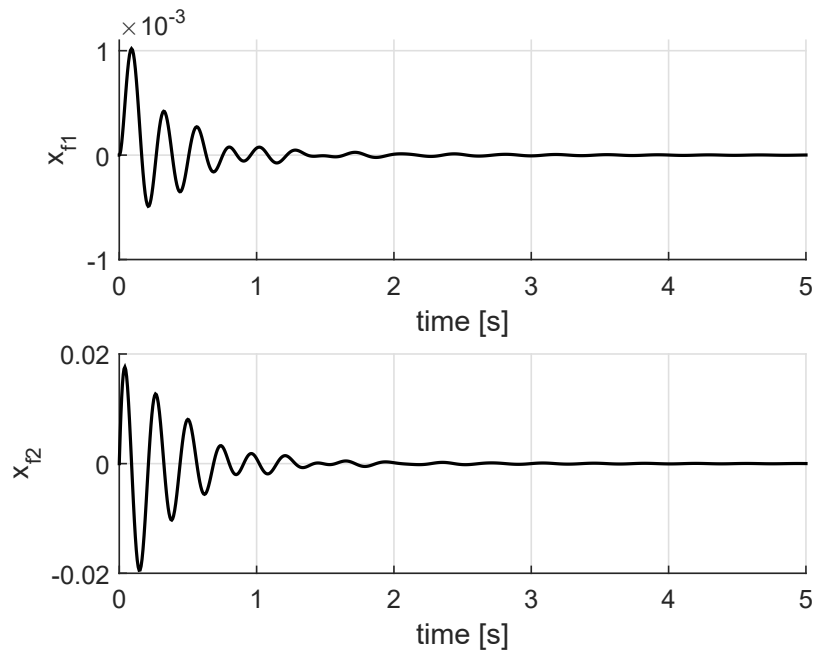
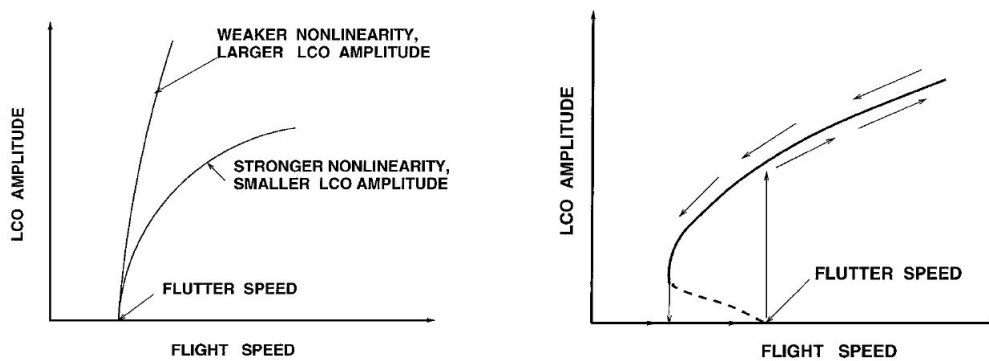


Figure 3.6: Aerodynamic states open loop response at  $U = 10$  m/s.

## 3.2 Generic Nonlinear Aeroelastic Behaviour

The structural fifth-order polynomial nonlinearity is introduced in the system to produce a nonlinear aeroelastic behavior; in this case, the nonlinear behaviour is a LCO. Of course, the LCO is not the only nonlinear behavior possible, but it is the main aeroelastic response phenomena and it is the simplest dynamic bifurcations that is possible to observe. A limit cycle is an isolated closed trajectory in the phase space. A stable, nonlinear system can exhibit self-sustained oscillations, as the one under investigation. Such system presents a stable limit cycle because all the trajectories in the phase plane converge on the limit cycle and remain even if slightly disturbed.

In general, in flight vehicles, the nonlinearities are not wanted, but LCO may be considered a "good" nonlinear behavior because may prevent a catastrophic flutter leading to loss of the flight vehicles [6].



(a) Nonlinearity leading to stable LCO.

(b) Nonlinearity leading to stable (solid line) and unstable (dotted line).

Figure 3.7: Schematic of LCO response [6].

The generic possibilities that can be observed in nonlinear aeroelastic behavior with LCOs are shown in Figure 3.7, in both of them the LCO amplitude is plotted vs airspeed. Figure 3.7(a) shows an aeroelastic system that is stable below the flutter velocity, independently by the small or large perturbations applied to the system. Beyond the flutter velocity, the LCO amplitude increases in a nonlinear way. The LCO amplitude depends by the nonlinearity present in the aeroelastic system: if the nonlinear stiffness coefficients are all compared to the stiffness of the related DOF, the LCO amplitude may become large and, arrived at certain airspeed, it may be possible to observe divergence of the system. On the other hand, if the nonlinearity is bigger and so are the polynomial coefficients, the LCO amplitude is smaller and the divergence occurs at higher airspeed. Figure 3.7(b) shows the other cases where the

onset of the LCO occurs below the flutter velocity, this happens if the perturbation applied to system is large enough. Now two LCOs exist at the same time: the stable (solid line), and unstable one (dotted line). Stable LCOs exist when, for any perturbation, the system returns to the same LCO. Instead, a system undergoing an unstable LCO, if disturbed moves away from the unstable LCO towards the stable LCO. In Figure 3.7 the arrows show the system behavior when the airspeed is increased or decreased. The system under investigation show an LCO below flutter velocity, called subcritical LCO [6].

In theory, if there are not perturbations, both stable and unstable LCOs are possible dynamics. It is also possible to notice the hysteretic response in the amplitude; it increases and then decreases. The consequences LCO of on a flying vehicle are the reduced vehicle performances and airframe structural fatigue (usually LCO amplitude does not reach the structural failure limits) [6].

### 3.2.1 Nonlinear System Behaviour

A nonlinear system can have different point of equilibrium as LCO; in general, a divergence from the origin can conduct a nonlinear system towards instability or towards another attractor. Once added the hardening nonlinearity, Eq. (3.1), to the linear model, the nonlinear aeroelastic model shows convergency, towards the state origin, behaviour analogous to the linear case below the critical velocity. Above flutter velocity, an initial small perturbation leads to a self sustained oscillation, that is an LCO. The hardening non linearity added to the plunge DOF is:

$$k_h(h) = k_0 + k_2h^2 + k_4h^4 = 3700.67 + 1.0657e8h^2 + 1.2760e12h^4 \quad (3.1)$$

where the estimated parameters are presented in table 2.4; they are converted from N/mm in the table, to N/m in the polynomial in Eq. (3.1).

The onset of the LCO for the numerical model occurs at 16 m/s and is induced by an initial perturbation of 5 deg applied to the pitch DOF. While experimentally, the onset occurs at a lower velocity, around 12.5 m/s. During the numerical simulations has been notice that the onset of the LCO does not occur below the flutter velocity if the initial perturbation on the pitch DOF is lower then 5 deg, in this case the LCO occurs at the flutter velocity. Furthermore, if the initial perturbation is too big the system reached the divergence before the LCO is established. An error always present in the experimental simulation is the free-play effects of the flap, in fact there will always be some rotation of the flap also if it is not actuated, in these study the freeplay model is not included in the analysis.

Phase portraits and time domain LCO diagrams have been compared between the numerical and experimental results. Figure 3.8 shows the comparison of the plunge and pitch time domain LCO diagrams. It is possible to notice that there

is a small difference in the LCO frequency and by a Fourier analysis on the LCO responses, the oscillation frequencies for the numerical 4.3 Hz and the experimental cases 4.4 Hz are obtained. The LCO frequencies for the two DOFs are identical, both for the experimental LCO and for the numerical one. The numerical and experimental differences can be attributed to differences in the underlying linear model at increasing airstream velocity. Moreover, it is possible to notice that, if the numerical LCO is symmetric for both DOFs, only the experimental pitch LCO is symmetric, while the experimental plunge LCO is not. At last, it is also noticed that the experimental LCOs amplitudes are bigger than the predicted ones [1]. It is important to mention that plunge and pitch present the same frequency but they are out of phase, as shown in Figure 3.9. By considering the phase of the plunge null it is possible to calculate the out of phase of the pitch, that has a value of more than 50 deg at 17 m/s.

Figure 3.10 shows the comparison of the plunge and pitch phase portraits; similar consideration can be drawn. Figure 3.8 shows some differences in the LCOs amplitude, the biggest differences are present in the plunge phase portrait, but the shape is quite well represented. Instead, the pitch phase portrait is a good matching for the LCO amplitude but the shape is less regular. This may be due to a non perfectly polynomial nonlinearity being introduced in the experimental model. Due to rig limitations, it is possible that the pretensioned wire exhibits a loose behaviour in the near-zero-displacement region [1].

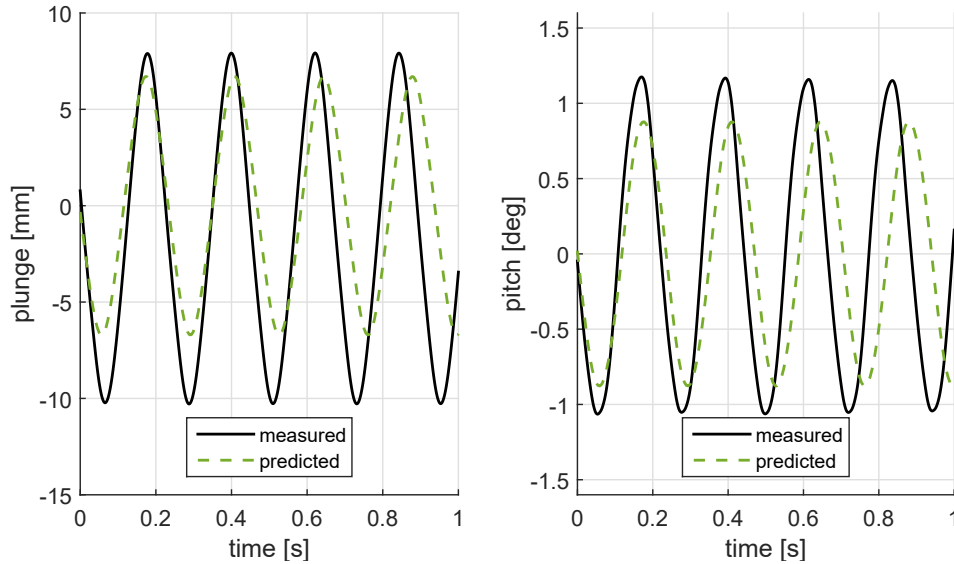


Figure 3.8: Time domain LCO diagrams - numerical vs experimental.

The aeroelastic system presents a LCO below the flutter velocity, the onset of

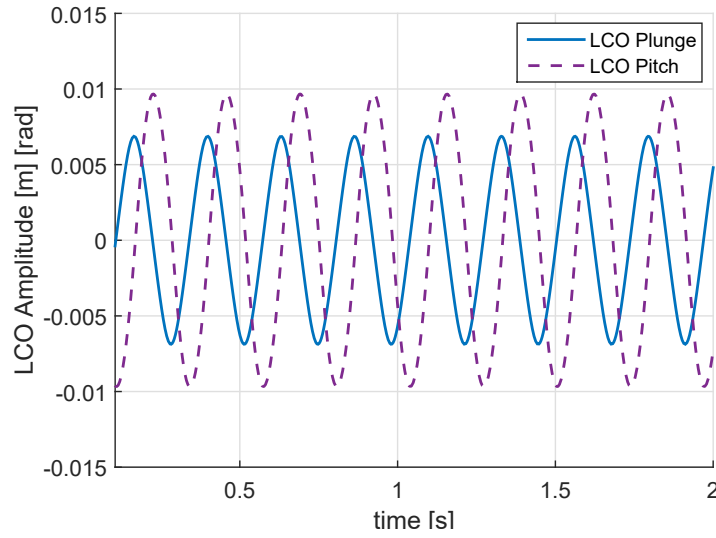


Figure 3.9: Phase displacement between pitch and plunge.

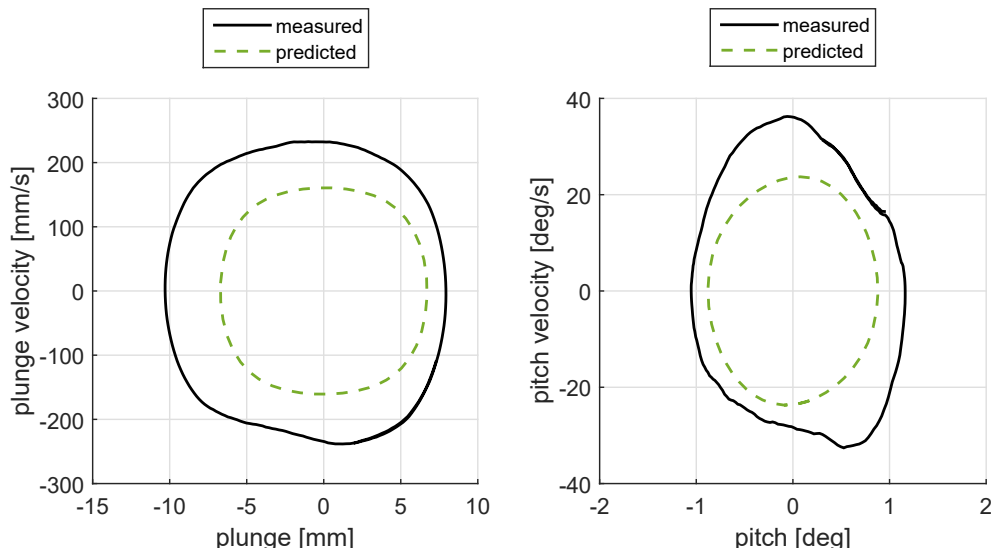


Figure 3.10: Phase portraits - numerical vs experimental.

the LCO occurs for 16 m/s for the numerical model, instead the flutter velocity is at 20 m/s. The system presents a subcritical point, and it may be observed an unstable LCO. It is important to note that the signs of the nonlinear stiffness terms in the polynomial, Eq.(3.1), that describe the structural nonlinearity added in the plunge DOF, are all positive. Referring to the literature, a subcritical bifurcation was

not expected because the coefficients are all positive, the system should be stable until the flutter velocity, as Figure 3.7(b). Referring to the literature, for observing a subcritical point in the aeroelastic system one or more stiffness term should be negative, usually the negative term is  $k_{h2}$ . In the case studied it is possible observe an unstable LCO also if all the stiffness terms in the polynomial nonlinearity are positive.

### 3.3 Subcritical bifurcation point

In this section the study of the bifurcation point is presented exposed. As already explained, the onset of the LCO occurs before the flutter velocity, so the system presents a subcritical behavior. The subcritical bifurcation point indicates the presence of an unstable behavior of the system. From the stable behavior of the system, shown in Figure 3.7, we suppose that the system presents an unstable LCO, as explain in the Section 3.2. For describing the unstable branch in the graphics airspeed-LCO amplitude it is necessary apply the describing function method: it is an approximate method for analyzing nonlinear system, it is based on quasi-linearization of the nonlinear system under investigation, it is one of the widely used method for analyzing limit cycle in closed-loop controllers.

#### 3.3.1 The describing function method

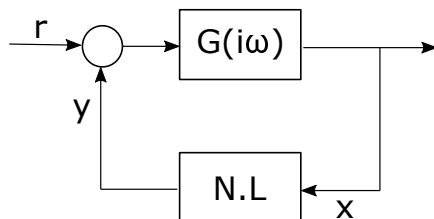


Figure 3.11: Feedback connection [10].

All the systems behavior is nonlinear and they could be describing as linear only for small perturbation. The describing function method allows studying the existence of periodic solution for Single-Input-Single-Output (SISO) system. It is possible to apply this method if the nonlinear physical system can be presented as a feedback connection of a linear dynamical system and a nonlinear element. Considering the SISO nonlinear system presented in Figure 3.11, we assume:

1. the external input is null ( $r=0$ ),
2. the nonlinearity is in algebraic form, time-invariant and memoryless,

3. the linear element is a strictly proper rational transfer function.

For studying the existence of periodic solution, it is assumed that such solution satisfies  $x(t + 2\pi/\omega) = x(t)$  for all  $t$ , where  $\omega$  is the frequency of oscillation. The general method for finding periodic solutions is usually called the *harmonic balance method*. The idea of the method is to represent a periodic solution by a Fourier series and seek a frequency  $\omega$  and a set of Fourier coefficients that satisfy the system's equation. For simplifying the exposition, we consider a sinusoidal input to the nonlinearity:

$$x(t) = X \sin(\omega t) \quad (3.2)$$

The nonlinearity output is a periodic solution with the same input frequency  $\omega$ , that can be written as a Fourier series:

$$y(t) = \sum_{n=1}^{\infty} (a_n \cos(n\omega t) + b_n \sin(n\omega t)) \quad (3.3)$$

where

$$a_n = \frac{1}{\pi} \int_{-\pi}^{\pi} y(t) \cos(n\omega t) d(\omega t) \quad b_n = \frac{1}{\pi} \int_{-\pi}^{\pi} y(t) \sin(n\omega t) d(\omega t)$$

There are no constant terms because the output is assumed symmetric respect the origin.  $a_n$  and  $b_n$  depend on the input signal amplitude  $X$ . We take the first harmonic of  $y(t)$ :

$$y(t) \simeq Y_1(X) \sin(\omega t + \varphi_1(X)) \quad (3.4)$$

where:

$$Y_1 = \sqrt{a_1^2 + b_1^2} \quad \varphi_1 = \arctan\left(\frac{a_1}{b_1}\right)$$

We considered only the first harmonic for two main reasons: higher harmonic amplitudes usually are smaller than the first and the linear part of the system is a low-pass filter, so it reduces the amplitude of the higher harmonic.

In order that the system presents a LCO, it has to satisfy the equation:

$$F(X)G(i\omega) + 1 = 0 \quad (3.5)$$

This equation is known as harmonic balance equation. The function  $F(X)$  defined as:

$$F(X) = \frac{1}{X} (b_1(X) + ia_1(X)) = \frac{1}{X} Y_1(X) \exp^{i\varphi_1(X)} \quad (3.6)$$

that is the *describing function* of the nonlinearity. Such describing function is obtained by applying a sinusoidal signal at the input of the nonlinearity and by calculating the ratio of the Fourier coefficient if the first harmonic is the output. It can be seen as an equivalent gain of a linear time invariant element [10].

The describing function method states that if Eq. (3.5) has a solution, then there is probably a periodic solution of the system with frequency and amplitude near the describing function ones. Conversely, if Eq. (3.5) has no solution, then the system probably does not have a periodic solution [10].

### 3.3.2 Application describing function method

We already know the stable output of the system, they were obtained calculating the solution of the nonlinear system. Applying the describing function method we expected to get the unstable output of the system. We study the state space model Eq. (1.25) but considering the relations between the states, it is sufficient considered three of them, rearranging Eq. (1.25), we can write:

$$\ddot{h} - q_1 h - q_2 \alpha - p_1 \dot{h} - p_2 \dot{\alpha} - r_1 x_{f1} - r_2 x_{f2} - f_{nl1} \psi(h) = 0 \quad (3.7)$$

$$\ddot{\alpha} - q_3 h - q_4 \alpha - p_3 \dot{h} - p_4 \dot{\alpha} - r_3 x_{f1} - r_4 x_{f2} - f_{nl3} \psi(h) = 0 \quad (3.8)$$

$$\dot{x}_{f2} - U\alpha - \dot{h} - b(0.5 - a)\dot{\alpha} + b_0 \frac{U^2}{b^2} x_{f1} + b_1 \frac{U}{b} x_{f2} = 0 \quad (3.9)$$

where  $\psi(h) = k_2 h^3 + k_4 h^5$  is the nonlinearity of the system. It is polynomial, memoryless and time-invariant, so it observes all the conditions assumed. Furthermore, the system can be represented by the feedback connection of Figure 3.11, so it is possible apply the describing function method.

In this case, three equations are considered that describe plunge, pitch and aerodynamic behavior, so three inputs are needed, we take the first harmonic of each input and we choose the time origin in way that we can assume the phase of the first harmonic of the plunge equal to zero:

$$h = A_h \cos(\omega t) \longrightarrow \dot{h} = -A_h \omega \sin(\omega t) \longrightarrow \ddot{h} = -A_h \omega^2 \cos(\omega t)$$

$$\alpha = A_\alpha \cos(\omega t + \varphi_\alpha) \longrightarrow \dot{\alpha} = -A_\alpha \omega \sin(\omega t + \varphi_\alpha) \longrightarrow \ddot{\alpha} = -A_\alpha \omega^2 \cos(\omega t + \varphi_\alpha)$$

$$x_{f2} = A_x \cos(\omega t + \varphi_x) \longrightarrow -A_x \omega \sin(\omega t + \varphi_x) \longrightarrow x_{f1} = \frac{A_x}{\omega} \sin(\omega t + \varphi_x)$$

There are six unknown: three amplitudes ( $A_h, A_\alpha, A_x$ ), two phases ( $\varphi_\alpha, \varphi_x$ ) and frequency ( $\omega$ ). Substituting the input and their derivatives in Eq. (3.9) and focusing the attention only on the structural nonlinearity, gives:

$$f_{nl1} \left( A_h^3 k_2 \cos^3(\omega t) + A_h^5 k_4 \cos^5(\omega t) \right) \quad (3.10)$$

$$f_{nl3} \left( A_h^3 k_2 \cos^3(\omega t) + A_h^5 k_4 \cos^5(\omega t) \right) \quad (3.11)$$

It is possible to replace the nonlinear trigonometric elements:

$$\begin{aligned}\cos^3(\alpha) &= \frac{3}{4} \cos(\alpha) + \frac{1}{4} \cos(3\alpha) \\ \cos^5(\alpha) &= \frac{5}{8} \cos(\alpha) + \frac{5}{16} \cos(3\alpha) + \frac{1}{16} \cos(5\alpha)\end{aligned}$$

Where the harmonics higher than the first one are negligible; considering only the first harmonic is not too restrictive because the LCOs shapes are smooth and they are centered in the origin, then the higher harmonics do not affect the behavior of the system. Replacing the rewritten nonlinearity and colleting  $\cos(\omega t)$  and  $\sin(\omega t)$  gives six equations, two for each original one:

$$\begin{aligned}-A_h\omega^2 - q_1A_h - q_2A_\alpha \cos \varphi_\alpha + p_2A_\alpha\omega \sin \varphi_\alpha - r_1\frac{A_x}{\omega} \sin \varphi_x - r_2A_x \cos \varphi_x \\ - \frac{3}{4}f_{nl1}A_h^3k_2 - \frac{5}{8}f_{nl1}A_h^5k_4 = 0\end{aligned}\quad (3.12)$$

$$-q_2A_\alpha \sin \varphi_\alpha + p_1A_h\omega + p_2A_\alpha\omega \cos \varphi_\alpha - r_1\frac{A_x}{\omega} \cos \varphi_x - r_2A_x \sin \varphi_x = 0\quad (3.13)$$

$$\begin{aligned}-A_\alpha\omega^2 \cos \varphi_\alpha - q_3A_h - q_4A_\alpha \cos \varphi_\alpha + p_4A_\alpha\omega \sin \varphi_\alpha - r_3\frac{A_x}{\omega} \sin \varphi_x - \\ r_4A_x \cos \varphi_x - \frac{3}{4}f_{nl3}A_h^3k_2 - \frac{5}{8}f_{nl3}A_h^5k_4 = 0\end{aligned}\quad (3.14)$$

$$\begin{aligned}-A_\alpha\omega^2 \cos \varphi_\alpha + q_4A_\alpha \sin \varphi_\alpha + p_3A_h\omega + p_4A_\alpha\omega \cos \varphi_\alpha \\ - r_3\frac{A_x}{\omega} \cos \varphi_x - r_4A_x \sin \varphi_x = 0\end{aligned}\quad (3.15)$$

$$\begin{aligned}-A_x\omega \sin \varphi_x - A_\alpha U \cos \varphi_\alpha + b(0.5 - a)A_\alpha\omega \sin \varphi_\alpha \\ + b_0\frac{U^2}{b^2}\frac{A_x}{\omega} \sin \varphi_x + b_1\frac{U}{b}A_x \cos \varphi_x = 0\end{aligned}\quad (3.16)$$

$$\begin{aligned}-A_x\omega \cos \varphi_x - A_\alpha U \sin \varphi_\alpha + A_h\omega + b(0.5 - a)A_\alpha\omega \cos \varphi_\alpha \\ + b_0\frac{U^2}{b^2}\frac{A_x}{\omega} \cos \varphi_x - b_1\frac{U}{b}A_x \sin \varphi_x = 0\end{aligned}\quad (3.17)$$

There are six equations with six unknown, then the system is solvable in a closed form. By solving the system we obtain only the two stable solutions shown in Figures 3.12 and 3.13. The system was solved in different ways, but the unstable solution was not found. One of the possible reasons is that the unstable solution, is not an LCO. There is certainly an unstable behavior of the system that connect the stable LCO to the stationary condition of the system, and its study will be the aim of future studies.

Figures 3.12 and 3.13 show the stable solutions of the system: the solution at zero amplitude and at the amplitude of the established LCO, these amplitudes are the same that were observe in predicted LCO in Figure 3.8. The arrows show denote path of the system response when flight speed is increasing or decreasing. As already said, in the figures we can notice that the onset of the LCO occurs at 16 m/s and the flutter velocity at 20.3 m/s. At the flutter velocity the amplitudes of both DOFs up from zero to the amplitude of the LCO. Figure 3.12 shows the amplitude of the plunge LCO that remain constant when decreasing the velocity, and slightly decrease near 16 m/s, while the amplitude pitch LCO increase while decreasing the velocity as shown in Figure 3.13. In both case the trends in the figure are as expected.

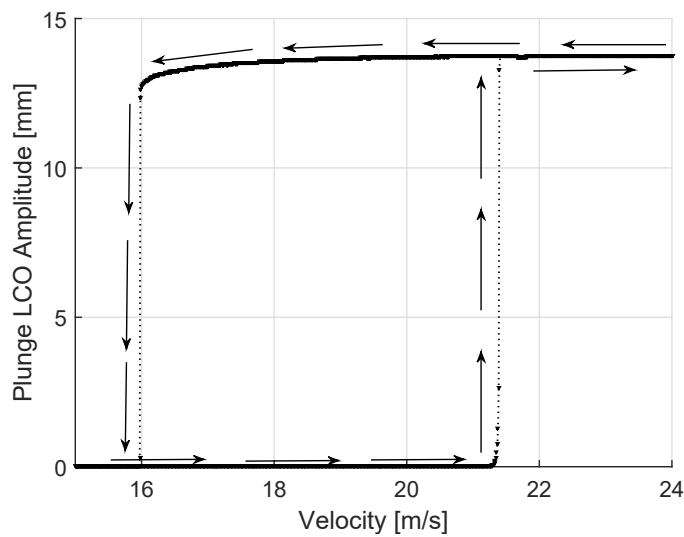


Figure 3.12: Plunge LCO amplitude.

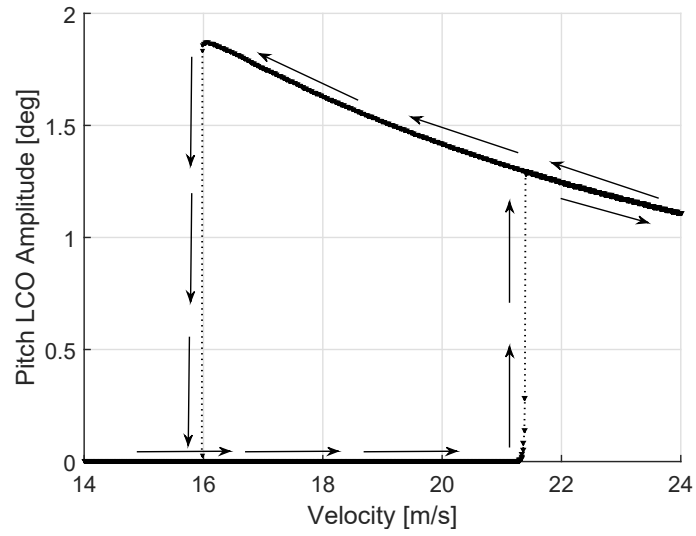


Figure 3.13: Pitch LCO amplitude.

Figure 3.14 and 3.15 show the frequency of the LCOs vs airspeed, the plunge and pitch LCO frequency are the same, the two graphs fit perfectly, as it is possible see in the figures.

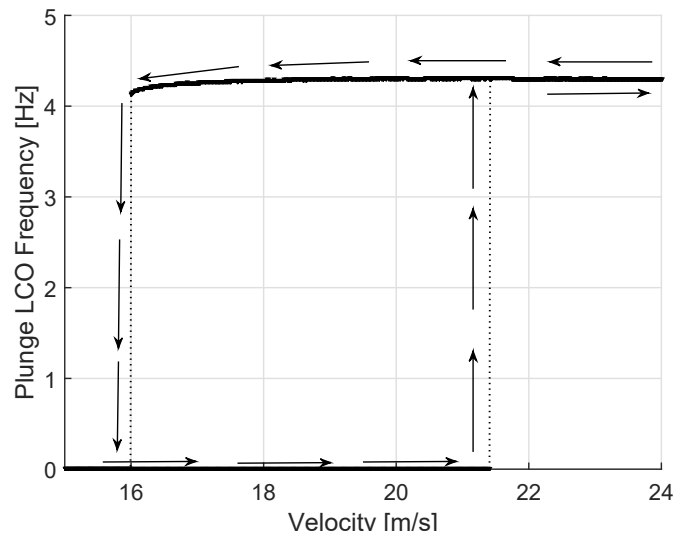


Figure 3.14: Plunge LCO frequency.

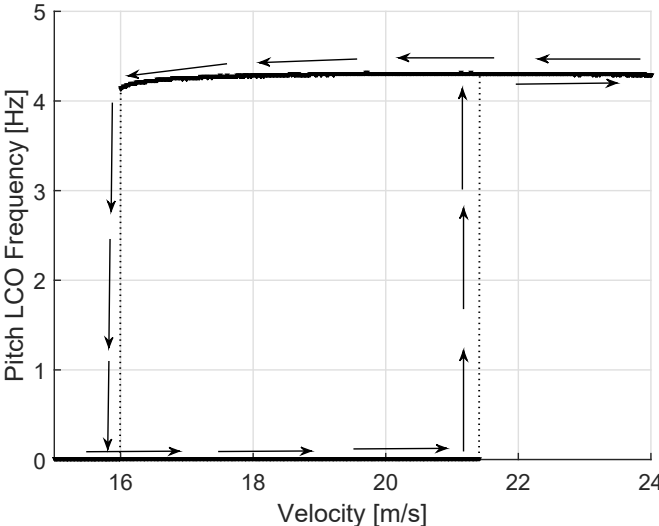


Figure 3.15: Pitch LCO frequency.

# Chapter 4

## Control Design and Closed-Loop Behaviour

In this chapter the derivation of the control design used on the system is presented. For controlling the system we consider a feedback linearization, described in Section 4.1. A coordinates transformation to make the system linearisable is shown along with the design of a nonlinear controller to cancel the nonlinearity. In the second part of the chapter the design of the control is presented. A schematic of control strategy is explained that we used to build the Simulink project then it is coupled to the dSPACE real-time control system used for closed-loop control. At the end of the chapter the experimental validation of the control design is presented and the closed-loop behaviour of the system is studied. These topics are been already discussed in [1], but here they will be elaborated in more depth and expanded.

### 4.1 Feedback Linearization

The complete aeroelastic system is nonlinear, for this reason the feedback linearization approach is considered to make the system linear at first and then design a stabilizing linear controller. This techniques is an exact cancellation of all the term that introduced nonlinearity in a given nonlinear system. Let us consider:

$$\begin{aligned}\dot{x} &= f(x) + g(x)u \\ y &= h(x)\end{aligned}\tag{4.1}$$

The *relative degree* of the system can be seen as the number of times the output should be differentiated before a direct coupling between input and the output derivative occurs. In particular, taking Lie derivatives of  $h$  along the solution of the

system considered as long as the input  $u$  does not appear yields:

$$\begin{aligned} y &= h(x) \\ \dot{y} &= L_f h + (L_g h)u \\ \ddot{y} &= L_f^2 h + (L_g L_f h)u \\ &\vdots \\ y^{(r)} &= L_f^r h + (L_g L_f^{r-1} h)u \end{aligned}$$

The Lie derivatives is defined as: the derivative of  $y$  in the direction of  $x$ :  $L_f \phi_i = \frac{d\phi}{dx} \cdot x$ . So it is possible to define the relative degree as: *the smallest integer such that  $L_g L_f^{r-1} h$  is not zero.*

For a system with well defined relative degree it is possible to define the following feedback law:

$$u = \frac{-L_f^r h + v}{L_g L_f^{r-1} h} \quad (4.2)$$

Notice that, by applying the following change of coordinates

$$z = T(x) = [h(x), L_f h(x), \dots, L_f^{r-1} h(x)]^T \in \mathbb{R}^r \quad (4.3)$$

one can easily see that:

$$\dot{z} = Az + Bv \quad (4.4)$$

where  $v$  is a scalar auxiliary input and matrices  $A$  and  $B$  are given as:

$$A = \begin{bmatrix} 0 & 1 & 0 & \cdots & 0 \\ 0 & 0 & 1 & 0 & \vdots \\ \vdots & \vdots & \ddots & \ddots & \vdots \\ 0 & 0 & \cdots & 0 & 1 \\ 0 & 0 & \cdots & 0 & 0 \end{bmatrix} \quad B = \begin{bmatrix} 0 \\ \vdots \\ \vdots \\ 0 \\ 1 \end{bmatrix}$$

The equation (4.4) defines the state space equations of a chain of integrators and it can be controlled by applying standard linear systems synthesis techniques.

It is important to remarks that equation (4.3) defines, in general, a partial change of coordinates. If  $r < n$ ,  $n - r$  additional state equations are needed in order to describe the *inner dynamics* of the original system. If  $r = n$ ,  $z \in \mathbb{R}^n$  is the new state of the system.

When the relative degree is strictly less than the system's dimension, only a partial feedback linearization can be achieved by applying the equation transformation and then the feedback law Eq. (4.2). In fact Eq. (4.4) does not describe the dynamics of the whole system. In order to fully describe the dynamics of the original

system 4.1, but in different coordinates, one needs to specify  $n - r$  extra variables and compute their derivative. Then it is possible to choose a change of coordinates  $\hat{x} = [z, \xi]$  where  $z$  is specified in Eq. (4.3) and  $\xi \in \mathbb{R}^{r-n}$  is a function of  $x$  so that the resulting set of differential equation takes the *normal form*:

$$\begin{aligned}\dot{z} &= Az + Bv \\ \dot{\xi} &= \phi(\xi, z)\end{aligned}\tag{4.5}$$

It is important to notice that while  $z$ -equations are linear, the  $\xi$  equations are nonlinear but input independent. The internal dynamic are forced by the value of the output  $y$  and derivatives. Given the cascaded structure of the normal form, one way to design the control  $v$  is using standard linear synthesis techniques so that the upstream system is globally asymptotically stabilized to any desired equilibrium state. To ensure that overall cascade is stable we may assume that the  $\xi$ -subsystem (the internal dynamics) is input to state stable with respect to the input variable  $z$ . This type of assumption on the internal dynamics are usually called minimum-phase assumption. If the system is minimum phase then the overall system is asymptotically stable. This link between the internal dynamics of a linear system and the position of its zeroes in the complex plane proves that the notion of zeroes of a transfer function has a natural counter-part in the context of nonlinear systems. For this reason the internal dynamics when evolving autonomously, that is with  $z$  indentially zero, define the zero-dynamics.

## 4.2 Feedback Linearization Applied to the Aeroelastic System

The feedback linearization method is used for suppressing the LCO that occurs when the airspeed goes over a critical speed. The system under analysis here needs to be made linearisable via a transformation, as there does not exist an input capable of cancelling the nonlinearity. A system using trailing edge actuators as in [2] is partially feedback linearisable, while with both leading and trailing edge actuators it is possible to make an exact feedback linearization. Now it is needed to choose a system output,  $y$ , for partially linearizing respect to it. The output chosen here is the pitch variable  $y = \alpha$ , because it does not present structural nonlinearities.

The first step in feedback linearization controller design is finding the transformation  $T(x)$  that allows the linearization of the system

$$T(x) = \begin{Bmatrix} \phi_1(x) \\ \phi_2(x) \\ \phi_3(x) \\ \phi_4(x) \\ \phi_5(x) \\ \phi_6(x) \end{Bmatrix} \quad (4.6)$$

The correct expression for  $T(x)$  is derived by calculating the Lie derivatives of the output variable  $y(t)$ .

The output considered is:  $y = \phi_1 = x_2$  and calculating its derivative yields:

$$\dot{\phi}_1 = \frac{d\phi_1}{dx} \cdot \dot{x} = \frac{d\phi_1}{dx} \cdot (f(x) + g(x)) = L_f\phi_1 + L_g\phi_1 \quad (4.7)$$

Calculating separately the two derivatives, the first results:

$$L_f\phi_1 = \frac{d\phi_1}{dx} \cdot f(x) = [0 \ 1 \ 0 \ 0 \ 0 \ 0] \begin{Bmatrix} x_3 \\ x_4 \\ \vdots \end{Bmatrix} = x_4 \quad (4.8)$$

meanwhile the second term is zero:

$$L_g\phi_1 = \frac{d\phi_1}{dx} \cdot g(x) = [0 \ 1 \ 0 \ 0 \ 0 \ 0] \begin{Bmatrix} \vdots \\ g_3 \\ g_4 \\ \vdots \end{Bmatrix} = 0 \quad (4.9)$$

as expected the output derivative is:

$$\dot{\phi}_1 = x_4 = \phi_2 \quad (4.10)$$

Calculating the other derivatives, it is possible to determine the relative degree of the system with the selected output. Determining the second derivative reads:

$$\dot{\phi}_2 = \frac{d\phi_2}{dx} \cdot (f(x) + g(x)) = L_f\phi_2 + L_g\phi_2 \quad (4.11)$$

It can be noted that the second term is not zero:

$$L_g\phi_2 = \begin{bmatrix} 0 & 0 & 0 & 1 & 0 & 0 \end{bmatrix} \begin{Bmatrix} \vdots \\ g_3 \\ g_4 \\ \vdots \end{Bmatrix} = g_4 \quad (4.12)$$

this indicates that the relative degree of the system is equal to two.

Now it is necessary to find the remaining four derivatives, the transformation functions are defined such that  $L_g\phi_i = 0$  with  $i = 1, \dots, 6$ , it is possible to write the conditions as:

$$L_g\phi_3 = \begin{bmatrix} \frac{d\phi_3}{dx_1} & \frac{d\phi_3}{dx_2} & \frac{d\phi_3}{dx_3} & \frac{d\phi_3}{dx_4} & \frac{d\phi_3}{dx_5} & \frac{d\phi_3}{dx_6} \end{bmatrix} \begin{Bmatrix} \vdots \\ g_3 \\ g_4 \\ \vdots \end{Bmatrix} = 0 \quad (4.13)$$

$$L_g\phi_4 = \begin{bmatrix} \frac{d\phi_4}{dx_1} & \frac{d\phi_4}{dx_2} & \frac{d\phi_4}{dx_3} & \frac{d\phi_4}{dx_4} & \frac{d\phi_4}{dx_5} & \frac{d\phi_4}{dx_6} \end{bmatrix} \begin{Bmatrix} \vdots \\ g_3 \\ g_4 \\ \vdots \end{Bmatrix} = 0 \quad (4.14)$$

$$L_g\phi_5 = \begin{bmatrix} \frac{d\phi_5}{dx_1} & \frac{d\phi_5}{dx_2} & \frac{d\phi_5}{dx_3} & \frac{d\phi_5}{dx_4} & \frac{d\phi_5}{dx_5} & \frac{d\phi_5}{dx_6} \end{bmatrix} \begin{Bmatrix} \vdots \\ g_3 \\ g_4 \\ \vdots \end{Bmatrix} = 0 \quad (4.15)$$

$$L_g\phi_6 = \begin{bmatrix} \frac{d\phi_6}{dx_1} & \frac{d\phi_6}{dx_2} & \frac{d\phi_6}{dx_3} & \frac{d\phi_6}{dx_4} & \frac{d\phi_6}{dx_5} & \frac{d\phi_6}{dx_6} \end{bmatrix} \begin{Bmatrix} \vdots \\ g_3 \\ g_4 \\ \vdots \end{Bmatrix} = 0 \quad (4.16)$$

For  $\phi_3$ ,  $\phi_5$  and  $\phi_6$  we can choose:

$$\phi_3 = x_1 \quad (4.17)$$

$$\phi_5 = x_5 \quad (4.18)$$

$$\phi_6 = x_6 \quad (4.19)$$

These choices simplify the derivatives calculation, to  $\phi_3$  corresponds the plunge dof, to  $\phi_5$  and  $\phi_6$  corresponds the two additional state  $x_{f1}$  and  $x_{f2}$  respectively. The variables defined in Eq. (4.19) verify the conditions Eq. (4.13), Eq. (4.15) and Eq. (4.16). The second condition is verified for this transformation function:

$$\frac{d\phi_4}{dx_3}g_3 + \frac{d\phi_4}{dx_3}g_4 = 0 \quad \Rightarrow \quad \phi_4 = x_3g_4 - x_4g_3 \quad (4.20)$$

So the resulting transformation is:

$$T(x) = \begin{Bmatrix} \phi_1(x) \\ \phi_2(x) \\ \phi_3(x) \\ \phi_4(x) \\ \phi_5(x) \\ \phi_6(x) \end{Bmatrix} = \begin{Bmatrix} x_2 \\ x_4 \\ x_1 \\ g_4x_3 - g_3x_4 \\ x_5 \\ x_6 \end{Bmatrix} = \begin{Bmatrix} \alpha \\ \dot{\alpha} \\ h \\ g_4\dot{h} - g_3\dot{\alpha} \\ x_{f1} \\ x_{f2} \end{Bmatrix} \quad (4.21)$$

Applying the transformation to the the dynamic system:

$$\begin{Bmatrix} \dot{\phi}_1 \\ \dot{\phi}_2 \\ \dot{\phi}_3 \\ \dot{\phi}_4 \\ \dot{\phi}_5 \\ \dot{\phi}_6 \end{Bmatrix} = \begin{Bmatrix} \phi_2 \\ \Delta_1 \\ \frac{1}{g_4}\phi_4 + \frac{g_3}{g_4}\phi_2 \\ \Delta_2 \\ \phi_6 \\ \Delta_3 \end{Bmatrix} + \begin{Bmatrix} 0 \\ g_4 \\ 0 \\ 0 \\ 0 \\ 0 \end{Bmatrix} \beta \quad (4.22)$$

where

$$\Delta_1 = g_3\phi_3 + g_4\phi_1 + p_3\frac{1}{g_4}\phi_4 + \left(p_4 + \frac{g_3}{g_4}p_3\right)\phi_2 + r_3\phi_5 + r_4\phi_6 \quad (4.23)$$

$$\begin{aligned} \Delta_2 = & (g_4q_2 - g_3q_4)\phi_1 + \left(p_1g_3 + p_2g_4 - g_3\left(p_4 + p_3\frac{g_3}{g_4}\right)\right)\phi_2 \\ & + (g_4q_1 - g_3q_3)\phi_3 + \left(p_1 - p_3\frac{g_3}{g_4}\right)\phi_4 + r_3\phi_5 + r_4\phi_6 \end{aligned} \quad (4.24)$$

$$\Delta_3 = U\phi_1 - bU\phi_5 - b_1\phi_6 + \left(b\left(\frac{1}{2} + a\right) + \frac{g_3}{g_4}\right)\phi_2 + \frac{\phi_4}{g_4} \quad (4.25)$$

It is possible to split the overall system into two different subsystems: the first depends on the input  $\beta$ :

$$\begin{Bmatrix} \dot{\phi}_1 \\ \dot{\phi}_2 \end{Bmatrix} = \begin{Bmatrix} \phi_2 \\ \Delta_1 \end{Bmatrix} + \begin{Bmatrix} 0 \\ g_4 \end{Bmatrix} \beta \quad (4.26)$$

while the second subsystem is not effected explicitly by the input:

$$\begin{Bmatrix} \dot{\phi}_3 \\ \dot{\phi}_4 \\ \dot{\phi}_5 \\ \dot{\phi}_6 \end{Bmatrix} = \begin{Bmatrix} \frac{1}{g_4}\phi_4 + \frac{g_3}{g_4}\phi_2 \\ \Delta_2 \\ \phi_6 \\ \Delta_3 \end{Bmatrix} \quad (4.27)$$

and represents the internal dynamics or zero dynamics. It must be stable in order to guarantee the stability of the overall system. In fact it is dangerous for internal states of the system to grow unbounded, as there is not any external input that acts on the subsystem.

The feedback linearization is exploited with a control law of the form:

$$\beta = \Psi(x) + \Gamma(x) \cdot v \quad (4.28)$$

where

$$\Psi(x) = -\frac{\frac{d\phi_2}{dx}f(x)}{\frac{d\phi_2}{dx}g(x)} = -\frac{L_f\phi_2}{L_g\phi_2} \quad \Gamma(x) = \frac{1}{\frac{d\phi_2}{dx}} = \frac{1}{L_g\phi_2} \quad (4.29)$$

Applying the control law to the system:

$$\beta = \frac{-\Delta_{beta} + v}{g_4} \quad (4.30)$$

where  $\Delta_{beta}$  is given by:

$$L_f\phi_2 = \frac{d\phi_2}{dx}f(x) = [0 \ 0 \ 0 \ 1 \ 0 \ 0] f(x) = \Delta_{beta} \quad (4.31)$$

with

$$\Delta_{beta} = q_3 + f_{nl2}(x_1) + q_4x_2 + p_3x_3 + p_4x_4 \quad (4.32)$$

This control law linearizes the first subsystem Eq. (4.26), that becomes:

$$\begin{Bmatrix} \dot{\phi}_1 \\ \dot{\phi}_2 \end{Bmatrix} = \begin{bmatrix} 0 & 1 \\ 0 & 0 \end{bmatrix} + \begin{Bmatrix} 0 \\ 1 \end{Bmatrix} v \quad (4.33)$$

where  $v$  is an auxiliary input that can be designed using any linear control technique to guarantee the stability of the subsystem. In this case, a pole placement control strategy is adopted:

$$v = -\bar{f}_1\phi_1 - \bar{f}_2\phi_2 \quad (4.34)$$

where  $\bar{f}_1$  determines the closed loop natural frequency, whereas  $\bar{f}_2$  affects the closed loop damping.

### 4.2.1 Inner Dynamics

Zero dynamics must be stable to apply feedback linearization, so its stability has to be verified. The subsystem describing the inner dynamics of the system is defined in Eq. (4.27). The zero dynamics of the system are obtained by setting  $\phi_1 = 0$  and  $\phi_2 = 0$ , so it is necessary to nullify the terms corresponding to the linearized subsystem:

$$\begin{Bmatrix} \dot{\phi}_3 \\ \dot{\phi}_4 \\ \dot{\phi}_5 \\ \dot{\phi}_6 \end{Bmatrix} = \begin{Bmatrix} \frac{1}{g_4}\phi_4 \\ A_{43}\phi_3 + A_{44}\phi_4 + r_3\phi_5 + r_4\phi_6 \\ \phi_6 \\ \frac{1}{g_4}\phi_4 - bU\phi_5 - b_1\phi_6 \end{Bmatrix} \quad (4.35)$$

where

$$\begin{aligned} A_{43} &= g_4q_1 - g_3q_3 \\ A_{44} &= p_1 - p_3\frac{g_3}{g_4} \end{aligned}$$

Writing the system that described the inner dynamics in matrix form, we obtain:

$$\begin{Bmatrix} \dot{\phi}_3 \\ \dot{\phi}_4 \\ \dot{\phi}_5 \\ \dot{\phi}_6 \end{Bmatrix} = \begin{bmatrix} 0 & \frac{1}{g_4} & 0 & 0 \\ A_{43} & A_{44} & r_3 & r_4 \\ 0 & 0 & 0 & 1 \\ 0 & \frac{1}{g_4} & -bU & -b_1 \end{bmatrix} \begin{Bmatrix} \phi_3 \\ \phi_4 \\ \phi_5 \\ \phi_6 \end{Bmatrix} \quad (4.36)$$

The zero dynamics are linear, but simulating them at the same velocities chosen for the test validation in the wing tunnel (described in section 4.4). A stable response is obtained. In fact, the real parts of all eigenvalues of 4.36 are negative, so the inner dynamics of the system are stable. The stability of the inner dynamic guarantees only its local stability, but it is a necessary condition of the aeroelastic model.

### 4.2.2 Pole Placement via Feedback Linearization

In this section the pole placement control strategy is presented. This control strategy used to add damping to the poles associated with pitch mode, then adding damping the pole reconstructed for creating  $v$  and  $v$  is integrated in the control law Eq. (4.30). The feedback linearization decoupled the pitch DOF from the overall system because it is the output  $y$  choose at the beginning of the creation of the controller. The controller is implemented with a desired value of the pitch damping ration. In this case, the damping is increasing by a defined percentage. So when the pole si modified, in reality only the real part is changed with desired value, meanwhile the immaginary part unchanged respectto the open loop linear natural frequencies[8].

From Eq. (4.34) and Eq. (4.33) it is possible writing:

$$\begin{Bmatrix} \dot{\phi}_1 \\ \dot{\phi}_2 \end{Bmatrix} = \begin{bmatrix} 0 & 1 \\ -f_1 & -f_2 \end{bmatrix} \begin{Bmatrix} \phi_1 \\ \phi_2 \end{Bmatrix} \quad (4.37)$$

where  $f_1 = \omega_{CL}^2$  and  $f_2 = 2\zeta_{CL}\omega_{CL}$ . This system describes only the pitch motion, it is decoupled to the overall aeroelastic system. By modified the  $f_2$  gain, the desire  $\zeta_{CL}$  can be placed, as already write it is modified only pitch damping  $\zeta_{CL}$  and not the its natural frequency  $\omega_{CL}$ . In the partial feedback linearization the controller law executes two task: 1) cancellation of the feedback dynamics, 2) implementation of the pole placement, the linear control requirement.

It is important to note that Eq. (4.37) linearized only of the pitch DOF and not of the all state of the system. The stability of the other states that define the inner dynamics of the system are already verified [2].

### 4.3 Simulink Design

In this section the control strategy that is used in the aeroelastic system control-loop is presented. This control strategy is the same that it is applied in the constructions of the Simulink model of the control design. The Simulink model will be built and embedded in the data-acquisition/control system, in our case it is dSPACE.

The control law that will be applied in the system is the feedback linearization, whose theoretical part is explained in the previous section and where it is possible notice that controller will need the access to the states of the system in real time. If the structural states pitch and plunge can be calculated directly by the measurement and their velocities can be numerically derived, but the two aerodynamic states can not be measured directly, so it becomes necessary find another way. In this case the aerodynamic states are reconstructed in real-time by the last two-row of the state space model Eq. (1.25) [8]

$$\begin{aligned}\dot{x}_5 &= x_6 \\ \dot{x}_6 &= Ux_2 + x_3 + b(0.5 - a)x_4 - b_0x_5 - b_1x_6\end{aligned}$$

So the mathematical model has to embed in the experimental control loop. The compute flap deflection angle is sent to the numerical aeroelastic model that was embedded in the experimental one, which calculate in real-time the full state vector, the structural states, i.e. the first four element, are replaced by the measure value to set up an *hybrid* state vector [8]:

$$x = \left[ \underbrace{x_1 \quad x_2 \quad x_3 \quad x_4}_{\text{measured}} \quad \underbrace{x_5 \quad x_6}_{\substack{\text{compluted} \\ \text{real-time}}} \right]^T$$

This hybrid vector is then used to calculate the control input. Finally, the hybrid vector is sent back to the numerical aeroelastic model, which allows computation of the state vector at the next time step. Figure 4.1 shows a schematic of the control strategy that we applied in the Simulink design for creating the control law. In our case, the time step between the measurements is 0.001 s, so the control loop is evaluated once every time step. The time step can be considered small enough to guarantee small variation of the state variable that is calculated by the embedded numerical model. The time step is decided by dSPACE [8].

Below it the different steps necessary for obtaining the dSPACE output are outlined [8]:

1. The measurements of the three laser displacement sensors, whose position was explain in section 2.1, are read and filtered to remove noise into dSPACE.
2. From the filtered displacement plunge ( $x_1$ ) and pitch ( $x_2$ ) are calculated, and their velocity are numerically derived: plunge velocity ( $x_3$ ) and pitch velocity

- ( $x_4$ ). Through pitch and plunge displacements and lasers the flap rotation angle  $\beta$  is calculated.
3. The numerical aeroelastic model computes the full state vector  $x$ , thanks the structural states ( $x_1, x_2, x_3, x_4$ ) and the flap rotation angle obtained in real-time.
  4. The two aerodynamic states ( $x_5, x_6$ ) are selected from the full state vector  $x$ .
  5. The new hybrid vector is set up: by adding up the two aerodynamic state to the structural states.
  6. The input to the experimental system is calculated.
  7. The output from dSPACE is sent to the piezoelectric actuator of the flap to obtain the required rotation.

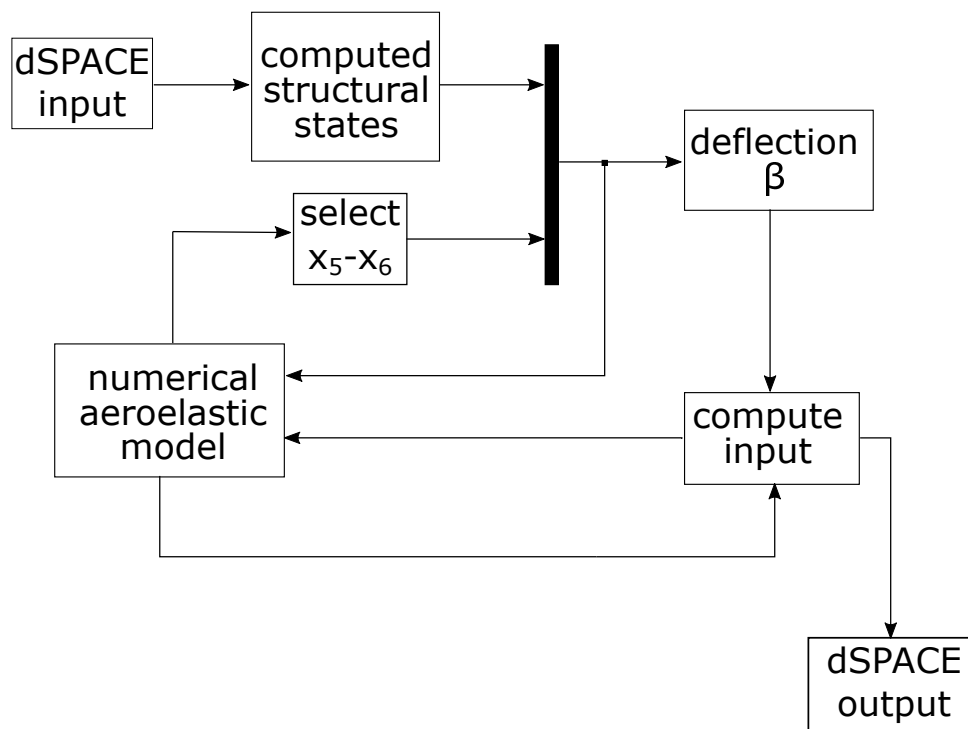


Figure 4.1: Schematic of control.

## 4.4 Closed-Loop Behaviour

In this section the closed loop behaviour of the system is presented. The feedback linearization method is applied to the system for suppressing the LCO that occurs when the airspeed goes over the critical speed of 16 m/s and the system is stabilized. The control design was presented in the last chapter, here the controller is applied on the test rig and validated.

Experimentally, the model was taken at the predetermined velocity and the LCO was excited by introducing a perturbation to the pitch DOF. Once the LCO was fully established, the controller was switched on and the data recorded [1]. For each case we considered, five different tests were done to enlarge a consistent outcome.

Four different cases were considered for the experimental validation. The test matrix is as follow:

1. Model undergoing LCO at 17 m/s, controller gain computed for 17 m/s with poles assigned with imaginary part unchanged respect to the open loop linear natural frequencies, real part increased of 10, 20 and 30%;
2. Model undergoing LCO at 15 m/s, controller gain computed for 17 m/s with poles assigned with imaginary part unchanged respect to the open loop linear natural frequencies, real part increased of 30%.
3. Model undergoing LCO at 15 m/s, controller gain computed for 15 m/s with poles assigned with imaginary part unchanged respect to the open loop linear natural frequencies, real part increased of 30%.
4. model undergoing LCO at 19 m/s, controller gain computed for 17 m/s with poles assigned with imaginary part unchanged respect to the open loop linear natural frequencies, real part increased of 30%.

The controller was built for the first test case with a damping increase of 30%. We would expect the controller to work at maximum efficiency in this case. Of course the controller should work in case of lower velocity, but we will verified if it works also for higher velocity. The controller is activated at the same time along an established LCO as in the experimental case, in this way it is possible a consistency in comparison, but in the numerical case less time is required for LCO decay.

Considering the first case, it is possible to compare the controller behaviour at different damping. Figures 4.2 and 4.3 show the controller stabilize the LCOs of both DOFs, plunge and pitch, in the first figure damping is increased of 10% instead in the second damping is increased of 20%, as the figures show the LCOs suppressed, but the decay time is the same for both damping considered. Meanwhile, in theory the time decay of the case with 10% additional damping should be longer than the case with 20% additional damping. For the first two damping considered there

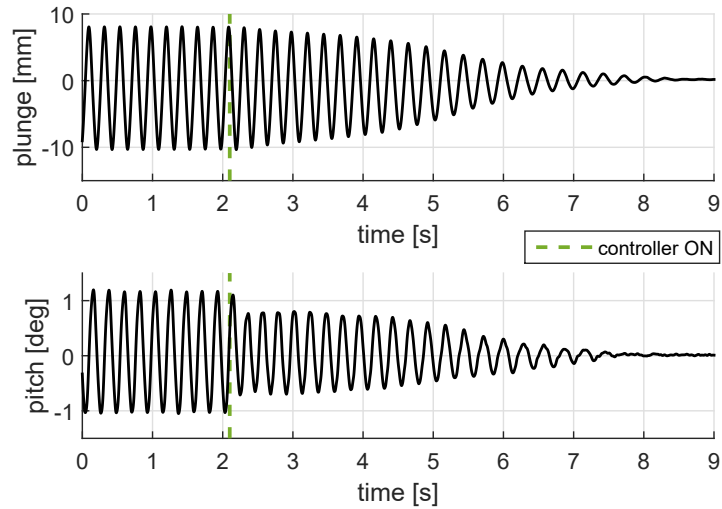


Figure 4.2: Test case 1: closed-loop response for 10% damping at 17 m/s.

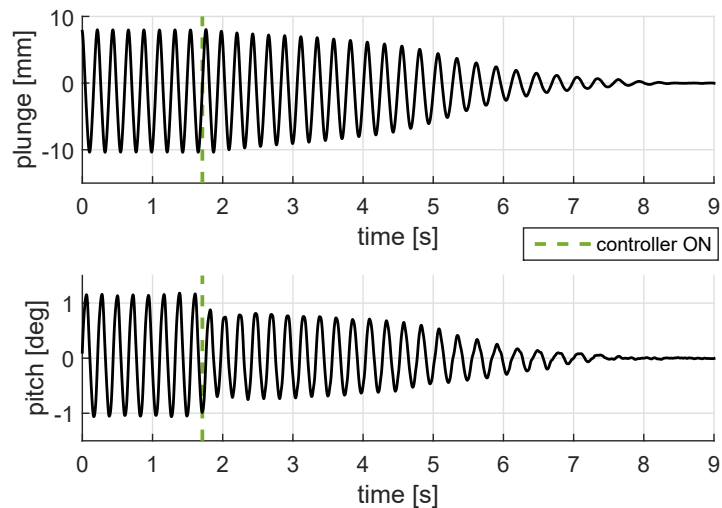


Figure 4.3: Test case 1: closed-loop response for 20% damping at 17 m/s.

are no differences in the closed-loop aeroelastic system response. Considering the highest damping (increased of 30%) in Figure 4.4, it is possible to note that the decay time is lower than the other cases, as expected. In all the cases the pitch decay time is slightly lower respect the plunge decay time, one reason for this could be that the nonlinearity is introduced in the plunge DOF.

Figure 4.4 shows the comparison between the numerical simulation and the experimental data for the test case with 30% additional damping. Both the numerical

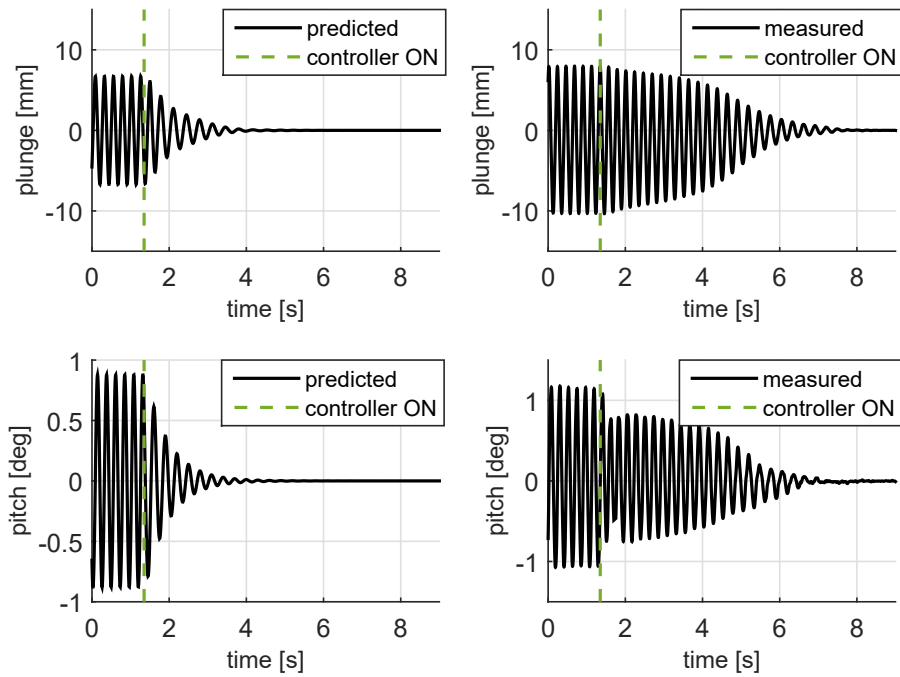


Figure 4.4: Test case 1: closed-loop response for 30% damping at 17 m/s.

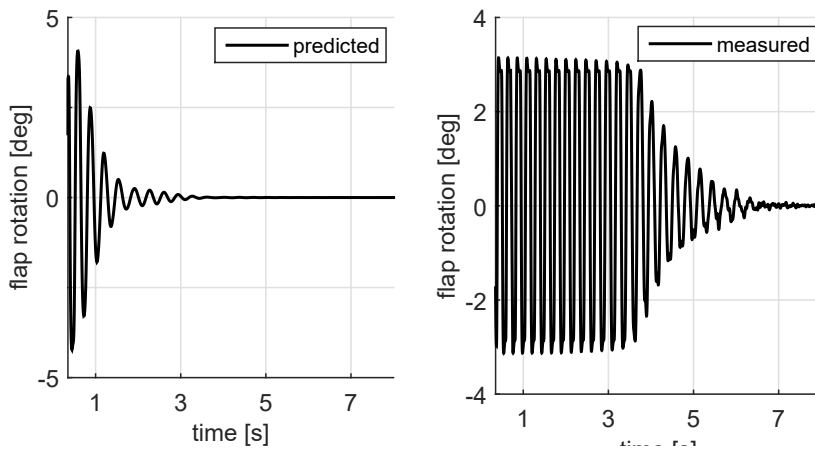


Figure 4.5: Test case 1: flap motion for closed-loop response for 30% damping at 17 m/s.

and the experimental controllers are capable of suppressing the established LCO. The decay time for the numerical simulation is 2s for both DOFs meanwhile for the experimental one is 5s [1]. A lot of reasons may be the causes for this discrepancy,

such as the loss of accuracy during the calculation of pitch and plunge deflections, and introduction of noise during numerical derivatives of pitch and plunge to obtain their velocity. Another reason could be the phase delays resulting from the filtering of signals that is required for numerical differentiation. Another major source of discrepancy could be the dynamics not being cancelled out completely, so the pitch motion is not uncoupled from the remaining dynamics, this is reflected in the nature of the measured pitch motion.

Figure 4.5 shows the comparison between the numerical and the experimental flap deflection. It can be seen that experimentally the flap experiences an initial region in which is saturated, due to the fact that the the control surface was commanded in open loop with a saturation of  $\pm 3$  deg, but it is still effective in reducing the LCO amplitude. Comparison between the fitted exponentials decays was done as well and shows a reasonable agreement in the region after the flap saturation [1]. Finally, it is possible to notice that the signal is not as smooth for negative amplitude as in the positive one. The reasons could be the asymmetry in the motion of the flap and freeplay.

Figures 4.6 and 4.8 show the cases 2 and 3, where the LCOs were established at 15 m/s. For these two cases no comparison with predictions is possible. Because, as already mentioned above in the mathematical model flutter occurs at 16 m/s. As it may be expected, the controller succeeds in supressing the LCO and the decay time is 3s, a time dacay slightly lower than the case 3, where the ad-hoc controller was used instead.

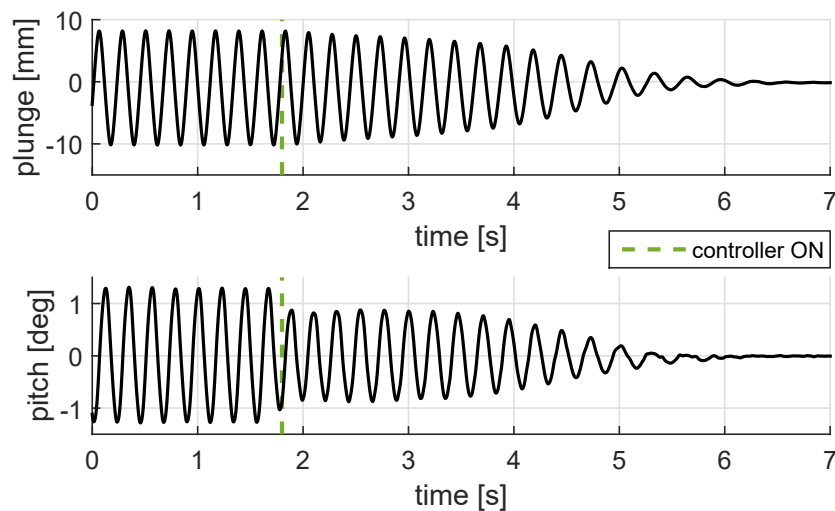


Figure 4.6: Test case 2: closed-loop response for 30% damping and controller gain computed for 17 m/s at 15 m/s.

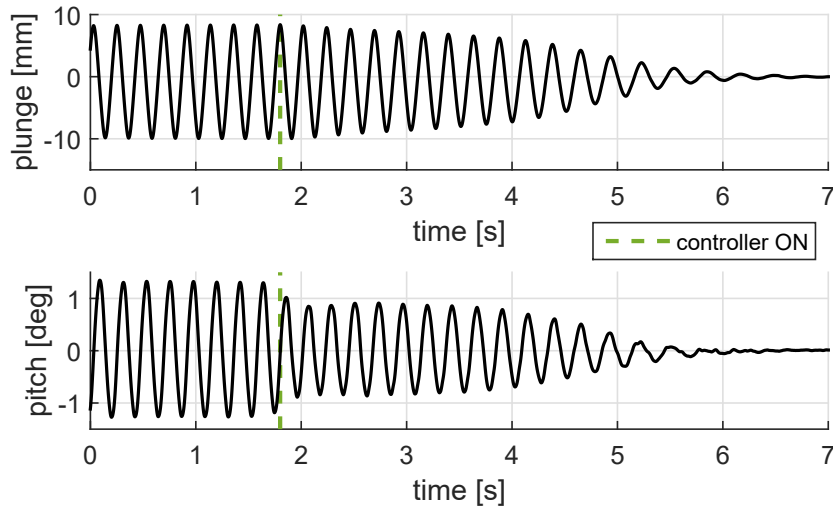


Figure 4.7: Test case 3: closed-loop response for 30% damping and controller gain computed for 15 m/s at 15 m/s.

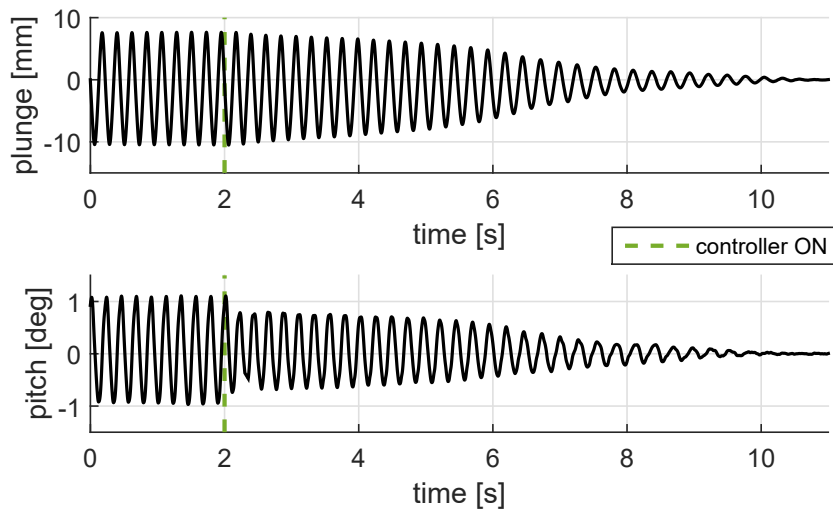


Figure 4.8: Test case 4: closed-loop response for 30% damping and controller gain computed for 17 m/s at 19 m/s.

The off-design controller is still capable of stabilising the system even at the higher airspeed velocity of 19 m/s. The flap presented a longer initial saturation and the decay time is increased to 8 s. So the system has a greater instability and is more complex to control. This behaviour is expected at inscreasing velocities as in this case. Moreover, initially the system seems to exhibit a beating behaviour that

may be due to the larger movement to the poles approaching the flutter velocity coupled with the attempt to place them to an off-design condition [1].



# Chapter 5

## Conclusions and Further Works

In this work a nonlinear rigid wing section model has been investigated. At the beginning, a mathematical model has been determined. It has been designed as a two DOFs plunge-pitch model since this is a choice widely used in the literature to describe the motion of rigid aerofoils. The structural-elastic equations have been determined via the Euler-Lagrange approach considering the kinetic and potential energies of the system in its motion. For the aerodynamic equations, Theodorsen theory has been used to describe an unsteady aerodynamic, but a filter was applied to write the system in space state. The resulting two DOFs plunge-pitch model is accurate to describe a rigid wing section and the unsteady aerodynamic has been verified by previous studies and the polynomial nonlinearity has also been confirmed by the literature

In Chapter 2, the experimental rig used in the experimental tests in the wind tunnel was described. Moreover, a method to obtain a numerical model describing the real system has been presented. Such a method has been applied on experimental data to adjust the model parameters so to fit the experimental system behaviour. Here the aim was to adjust the parameters of analytical FRFs to fit the experimental one. For this step, only the structural subsystem has been considered, i.e. all experimental and analytical FRFs have been calculated without aerodynamic part, so at zero airspeed. This fitting has been formulated as a nonlinear least squares problem; the initial parameters dataset has been calculated empirically and the an appropriate algorithm has been used to adjust the parameters dataset to minimize the least square error. Then the estimation of the nonlinear parameters has been carried out from a static force test. The fitting of the structural model has reached a good result with such dataset. So the tuning of the numerical model with the experimental FRFs is available approach.

In Chapter 3, the open-loop behaviour of the aeroelastic system has been studied. An analysis of the system eigenvalues has been made for increasing free-stream velocity in order to determine the flutter velocity. Then a fifth-order hardening

nonlinearity was introduced in the equation to describe the structural nonlinearity present in the real system. At the end, the overall system was obtained and it presented a bifurcation leading to an LCO. When the critical velocity is reached, the self-sustained oscillations of plunge and pitch DOFs occur. Two main differences has been observed between the model and the real system: the first is the different frequency between numerical and experimental ones. But the most relevant ones are the different amplitudes of the LCOs. However, the discrepancies are around 20-30 %, so the model turned out to be a fair description of the qualitative behaviour of the system. At the end, the subcritical bifurcation point has been studied by applying the describing function method for determining the unstable behaviour of the system. However, the unstable behaviour has not been determined, one reason could be that the unstable solution is not a periodic one and so it could not be determined via describing function method. In fact, with this method the two stable solution, at LCO established and at zero amplitude, has been determined with a good result.

In Chapter 4, the suppression of LCO by using the feedback linearization control strategy has been presented and the numerical simulations of the resulting controlled model has been reported. An output feedback linearization controller has been considered. This strategy is based on the design of an input to cancel the nonlinear part of the system so to stabilise it with a linear controller. In this case, it was only possible to linearize the system partially. So a coordinates transformation has been used to decompose the system into two subsystems. The first one can be made linear by using a designed input that cancels the nonlinearity. The second one does not depend on the input, and represents the inner dynamic, that tuned out asymptotically stable. As result, the controller stabilises the system suppressing the LCOs with good performances. In fact, the active control is capable of suppressing LCO in at the design airspeed and 15% below and above it.

Future research could usefully explore new improvements of the design control. Moreover the highlighted discrepancies in open-loop behaviour, especially the potential presence of a subcritical bifurcation leading to LCO should be investigated.

# Bibliography

- [1] Isnardi, Irma and Paoletti, Paolo and Miranda, Domenico and Innocenti, Giacomo and Fichera, Sebastiano, *Nonlinear Aeroservoelastic Control Design and Validation*, 2018 AIAA Guidance, Navigation, and Control Conference, Kissimmee, Florida, 8â12 January 2018.
- [2] Ko, Jeonghwan and Strganac, Thomas W and Kurdila, Andrew J, *Adaptive feedback linearization for the control of a typical wing section with structural nonlinearity*, *Nonlinear Dynamics*, 18, 289-301, 1999, Springer.
- [3] Block, Jeffrey J and Strganac, Thomas W, *Applied active control for a nonlinear aeroelastic structure*, *Journal of Guidance, Control, and Dynamics*, 6, 838-845, 1998.
- [4] Bhoir, Nilesh and Singh, Sahjendra N, *Output feedback nonlinear control of an aeroelastic system with unsteady aerodynamics*, *Aerospace science and technology*, 8, 195-205, 2004, Elsevier.
- [5] Hodges, Dewey H and Pierce, G Alvin, *Introduction to Structural Dynamics and Aeroelasticity: Second Edition*, Cambridge University Press, 2011.
- [6] Dowell, Earl H, *A modern course in aeroelasticity*, Springer, 2015.
- [7] Wright, Jan Robert and Cooper, Jonathan Edward, *Introduction to aircraft aeroelasticity and loads*, John Wiley & Sons, 2008.
- [8] Jiffri, Shakir and Fichera, Sebastiano and Mottershead, John E and Da Ronch, Andrea, *Experimental nonlinear control for flutter suppression in a nonlinear aeroelastic system*, *Journal of Guidance, Control, and Dynamics*, 1-14, 2017.
- [9] Da Ronch, Andrea and Tantaroudas, Nikolaos D and Badcock, Kenneth J and Mottershead, John, *A nonlinear controller for flutter suppression: from simulation to wind tunnel testing*, 55th AIAA/ASMe/ASCE/AHS/SC Structures, Structural Dynamics, and Materials Conference, 2014.
- [10] Khalil, Hassan K *Nonlinear System*, 3rd ed. Prentice Hall, 2002.
- [11] Ardelean, Emil Valentin and Clark, Robert L, *V-Stack Piezoelectric Actuator*, SPIE Smart Structures and Materials, 4333, 322-333, 2001.





UNIVERSITÀ  
DEGLI STUDI  
FIRENZE

Part of the thesis was developed with Prof. Giacomo Innocenti from the Information Department (DINFO) of Università di Firenze.

Dr Ing Giacomo Innocenti  
Dipartimento di Ingegneria  
dell'Informazione  
Universita' degli Studi di Firenze  
E: [giacomo.innocenti@unifi.it](mailto:giacomo.innocenti@unifi.it)  
T: 055 2758527

Commissione di Laurea  
Dipartimento di Ingegneria Meccanica e Aerospaziale  
Politecnico di Torino

Gentile Commissione di Laurea,

il mio studente Domenico Miranda ed il sottoscritto hanno avuto il piacere di collaborare con Irma Isnardi su parte del suo progetto di tesi. Tale attività è risultata in una presentazione alla conferenza AIAA Science and Technology Forum tenutasi ad Orlando (UK) in data 8-12 Gennaio 2018.

Con la presente confermo l'assenso da parte del team di Firenze all'inclusione nella tesi di Irma del materiale presentato a tale conferenza, in quanto Irma ha dato un contributo fondamentale nell'ottenimento dei risultati presentati.

Rimango comunque a disposizione per eventuali chiarimenti o ulteriori informazioni.

In fede,

Giacomo